AFRL-AFOSR-VA-TR-2022-0395

Studies of Electrode-Plasma Effects on Breakdown at RF Frequencies

Ravindra Joshi
TEXAS TECH UNIVERSITY SYSTEM
2500 BROADWAY
LUBBOCK, TX, 79409
USA

07/16/2022
Final Technical Report

Air Force Research Laboratory
Air Force Office of Scientific Research
Arlington, Virginia 22203
Air Force Materiel Command

REPORT DOCUMENTATION PAGE

PLEASE DO NOT RETURN YOUR FORM TO THE ABOVE ORGANIZATION.

1. REPORT DATE	**2. REPORT TYPE**	**3. DATES COVERED**	
20220716	Final	**START DATE** 20180101	**END DATE** 20220531

4. TITLE AND SUBTITLE
Studies of Electrode-Plasma Effects on Breakdown at RF Frequencies

5a. CONTRACT NUMBER	**5b. GRANT NUMBER**	**5c. PROGRAM ELEMENT NUMBER**
	FA9550-19-1-0056	61102F
5d. PROJECT NUMBER	**5e. TASK NUMBER**	**5f. WORK UNIT NUMBER**

6. AUTHOR(S)
Ravindra Joshi

7. PERFORMING ORGANIZATION NAME(S) AND ADDRESS(ES)	**8. PERFORMING ORGANIZATION REPORT NUMBER**
TEXAS TECH UNIVERSITY SYSTEM 2500 BROADWAY LUBBOCK, TX 79409 USA	

9. SPONSORING/MONITORING AGENCY NAME(S) AND ADDRESS(ES)	**10. SPONSOR/MONITOR'S ACRONYM(S)**	**11. SPONSOR/MONITOR'S REPORT NUMBER(S)**
Air Force Office of Scientific Research 875 N. Randolph St. Room 3112 Arlington, VA 22203	AFRL/AFOSR RTB1	AFRL-AFOSR-VA-TR-2022-0395

12. DISTRIBUTION/AVAILABILITY STATEMENT
A Distribution Unlimited: PB Public Release

13. SUPPLEMENTARY NOTES

14. ABSTRACT
The goals and objectives of this project focus on simulations and basic research for understanding fundamental details of processes at the cathode such as electron emission, outgassing, and breakdown under RF conditions for vacuum electronics and high power applications. Details relating the role of both photoemission and photoionization are included in the breakdown physics, with the former process shown to be dominant at atmospheric pressure. Other aspects such as space-charge, proximity- and density-dependent dynamic screening, out-gassing and plasma formation are probed based on many-body charge transport coupled with the Fast Multipole Method, as they all directly affect the efficiency and reliability of high power microwave (HPM) systems. Comprehensive electron emission included evaluations of material properties (e.g., workfunction), and internal potentials that were folded into the Schrodinger Wave Equation for transmission probability analysis. In addition, surface changes (e.g., oxide over-layer, adsorbates) that alter material work function, thus adversely impacting electron emission, are also studied based on Density Functional Theory. Additionally, the effort this year included simulations to study carbon fibers, which were shown to significantly reduce outgassing. Also, geometric variations in emitter structures from an atomistic standpoint, not just macroscopic field enhancements, were considered through numerical analysis. Finally, an important question that was addressed based on fundamental physics and materials science, was the role of adsorbates on the Secondary Electron Yield (SEY).

15. SUBJECT TERMS

16. SECURITY CLASSIFICATION OF:			**17. LIMITATION OF ABSTRACT**	**18. NUMBER OF PAGES**
a. REPORT	**b. ABSTRACT**	**c. THIS PAGE**		
U	U	U	UU	44

19a. NAME OF RESPONSIBLE PERSON	**19b. PHONE NUMBER** *(Include area code)*
JOHN LUGINSLAND	000-0000

Section 1: Structured Survey Questions

Award Information

- Award Number: FA9550-19-1-0056
- Report Type: Three-Year in Annual Increments
- Principal Investigator: Ravi P. Joshi
- Principal Investigator Email: ravi.joshi@ttu.edu
- Principal Investigator Phone: 806-834-7979
- Project Title: Studies of Electrode-Plasma Effects on Breakdown at RF Frequencies
- Recipient Organization: Texas Tech University
- Business Office Email: ors@ttu.edu
- Report Due Date: 08/29/2021
- Report Period Start Date 01/01/2019
- Report Period End Date 05/31/2022
- Current Program Officer: Dr. John Luginsland
- Please list any other Co-Program Officers (if applicable): N/A

Publications

1. M. Brown, M. Sanati, and R. P. Joshi, "Combined First Principles-Monte Carlo Analyses to Evaluate the Effect of Surface Hydrogen on the Secondary Electron Yield of Nickel," *Journ. Appl. Physics* **131**, 103301 (2022); DOI - 22); https://doi.org/10.1063/5.0080721.

2. S. N. Sami, R. Islam, S. Portillo, E. Schamiloglu, and R. P. Joshi, "Numerical Evaluations of Hydrogen Outgassing from Cesium Coated Carbon Fiber Electrodes," *Vacuum* **198**, 110869 (2022); DOI - https://doi.org/10.1016/j.vacuum.2022.110869.

3. S. N. Sami, R. Islam, and R. P. Joshi, "Atomistic calculations of thermal conductivity in films made from graphene sheets for electron emitter applications," *AIP Advances* **11**, 105310 (2021); DOI - https://doi.org/10.1063/5.0062044.

4. D. Guo, S. N. Sami, L. Diaz, S. Sanati, and R. P. Joshi, "Evaluation of Electron Currents from Cesium Coated Tungsten Emitter Arrays with Inclusion of Space Charge Effects, Workfunction Changes and Screening," *Journal of Vacuum Science and Technology B* **39**, 054201 (2021); DOI - https://doi: 10.1116/6.0001185.

5. S. N. Sami, R. Islam, R. Khare, and R. P. Joshi, "Simulations of hydrogen outgassing from carbon fibers," *Journal of Applied Physics* **129**, 213303 (2021); DOI - https://doi.org/10.1063/5.0054440.

6. D. Guo, W. Milestone, and R. P. Joshi, "Many-Particle based evaluations for maximum current output from bimodal electron emitter arrays," *Journal of Applied Physics* **129**, 173301 (2021); DOI - https://doi.org/10.1063/5.0047528.

7. S. N. Sami, M. Sanati, and R. P. Joshi, "Simulations of hydrogen outgassing and sticking coefficients at a copper electrode surface: dependencies on temperature, incident angle and energy," *Physical Review Research* **3**, 013203 (2021); DOI -

https://doi.org/10.1103/PhysRevResearch.3.013203.

8. S. N. Sami, L. Diaz, M. Sanati, and R. P. Joshi, "Simulations of Field Emission from Copper Electrodes with Inclusion of Oxygen Surface Layer and Work Function Changes Based on First-Principles Calculations," *Journ. Applied Physics* **128**, 223302 (2020); DOI: - 10.1063/5.0031568.

9. X. Qiu, L. Diaz, M. Sanati, J. Mankowski, J. Dickens, A. Neuber, and R. P. Joshi, "Coupled Analysis to Probe the Effect of Angular Assignments on the Secondary Electron Yield (SEY) from Copper Electrodes," *Physics of Plasmas* **27**, 093511 (2020); DOI: - https://doi.org/10.1063/5.0010389.

10. D. Guo, S. N. Sami, and R. P. Joshi, "Electron Emission from Metal Emitters Subject to a High Intensity Laser in the Presence of DC Electric Fields," *AIP Advances* **9**, 105302 (2019); DOI: -- https://doi.org/10.1063/1.5122212.

11. H. Nguyen, M. Sanati, and R. P. Joshi, "Probing Changes in Secondary Electron Yield from Copper Electrodes Due to Surface Defects and Changes in Crystal Orientation," *Journ. Appl. Phys.* **126**, 123301 (2019); DOI: -- https://doi.org/10.1063/1.5113642.

12. J. Acharjee and R. P. Joshi, "Numerical Evaluation of Hydrogen Outgassing from Copper Electrodes With Mitigation Based on a Tungsten Capping Layer," *Physics of Plasmas* **26**, 093504 (2019); DOI: -- https://doi.org/10.1063/1.5109682.

Submitted for Publication and Under Review

1. S. N. Sami, R. Islam, and R. P. Joshi, "Molecular Dynamics Simulation of Outgassing from Carbon Nanotubes," submitted for publication, 2022.

2. M. Brown, W. Milestone, and R. P. Joshi, "Monte Carlo Analysis of Electron Trapping in Nested Groove Structures for Mitigation of Secondary Electron Emission for Potential Multipactor Control in Waveguides," submitted for publication, 2022.

3. M. Brown, L. Diaz, A. Aslan, M. Sanati, S. Portillo, E. Schamiloglu, and R. P. Joshi, " Carbon-Oxygen Surface Formation Enhances Secondary Electron Yield in Cu, Ag and Au: A coupled first-principles, Monte Carlo Analysis," submitted for publication, 2022.

Participants

You will be asked to provide the information below for: (1) PIs; and (2) each person who worked on and was funded by this grant during the current reporting period. Please include all participants including yourself.

- Ravi P. Joshi, Principal Investigator.
- Total number of months (including partial months) worked on project: 6.
- ORCID: https://orcid.org/0000-0003-1554-9664.
- Project role: Was affiliated with and worked on the project during the entire January 2019 – May 2022 duration. The main roles included the following: advising students, project management, data analysis, planning future steps/directions and suggesting simulations, helping student with manuscript corrections, submission of manuscripts etc.

- Contribution to the project: 30%
- International business: None (N/A)

- Mahdi Sanati, Co-Principal Investigator.
- Total number of months (including partial months) worked on project: 4.5.
- ORCID: https://orcid.org/0000-0001-9855-4332.
- Project role: Was affiliated with and worked on the project during the entire January 2019 – May 2022 duration. The main roles included the following: project management, data analysis, planning future steps/directions and suggesting simulations, helping student with manuscript corrections, submission of manuscripts etc.
- Contribution to the project: 25%
- International business: None (N/A)

- Andreas Neuber, Co-Principal Investigator.
- Total number of months (including partial months) worked on project: 0.75.
- ORCID: https://orcid.org/ 0000-0002-9092-501X.
- Project role: Was affiliated with and worked on the project during the entire January 2019 – May 2022 duration. The main roles included the following: data analysis, planning future steps/directions and suggesting simulation work, helping student with manuscript corrections, submission of manuscripts etc.
- Contribution to the project: 5%
- International business: None (N/A)

- James Dickens, Co-Principal Investigator.
- Total number of months (including partial months) worked on project: 0.75.
- ORCID: https://orcid.org/ 0000-0001-9195-2821.
- Project role: Was affiliated with and worked on the project during the entire January 2019 – May 2022 duration. The main roles included the following: data analysis, planning future steps/directions and suggesting simulation work, helping student with manuscript corrections, submission of manuscripts etc.
- Contribution to the project: 5%
- International business: None (N/A)

- John Mankowski, Co-Principal Investigator.
- Total number of months (including partial months) worked on project: 0.75.
- ORCID: https://orcid.org/ 0000-0003-3723-8672.
- Project role: Was affiliated with and worked on the project during the entire January 2019 – May 2022 duration. The main roles included the following: data analysis, planning future steps/directions and suggesting simulation work, helping student with manuscript corrections, submission of manuscripts etc.
- Contribution to the project: 5%
- International business: None (N/A)

- S. N. Sami, Ph.D. student.
- Total number of months (including partial months) worked on project: 26
- ORCID: https://orcid.org/ 0000-0002-8972-1909.
- Project role: Was affiliated with and worked on the project during the entire January 2019 – May 2022 duration. The main roles included the following: setting up simulations, data analysis, helping student with manuscript preparation, carrying out day-to-day research activities and simulations.
- Contribution to the project: 30%
- International business: None (N/A)

Other Partners or Collaborators

None (N/A)

Inventions, patent applications, licenses, and technologies/techniques

- Patents
  - None.
- Inventions
  - None.
- Licenses
  - None.
- Technologies or Techniques
  - None (N/A).
- Other Products
  - None (N/A).

This work was sponsored by the Air Force Office of Scientific Research (AFOSR), under grant FA9550-19-1-0056. The views and conclusions contained herein are those of the authors only and should not be interpreted as representing those of AFOSR, the U.S. Air Force, or the U.S. Government.

Section 2: Technical Report

Distribution Statement - *This report is cleared for public release through Texas Tech University's processes and procedures.*

Abstract - The goals and objectives of this project focus on simulations and basic research for understanding fundamental details of processes at the cathode such as electron emission, outgassing, and breakdown under RF conditions for vacuum electronics and high power applications. Details relating the role of both photoemission and photoionization are included in the breakdown physics, with the former process shown to be dominant at atmospheric pressure. Other aspects such as space-charge, proximity- and density-dependent dynamic screening, outgassing and plasma formation are probed based on many-body charge transport coupled with the Fast Multipole Method, as they all directly affect the efficiency and reliability of high power microwave (HPM) systems. Comprehensive electron emission included evaluations of material properties (e.g., workfunction), and internal potentials that were folded into the Schrodinger Wave Equation for transmission probability analysis. In addition, surface changes (e.g., oxide over-layer, adsorbates) that alter material work function, thus adversely impacting electron emission, are also studied based on Density Functional Theory. Additionally, the effort this year included simulations to study carbon fibers, which were shown to significantly reduce outgassing. Also, geometric variations in emitter structures from an atomistic standpoint, not just macroscopic field enhancements, were considered through numerical analysis. Finally, an important question that was addressed based on fundamental physics and materials science, was the role of absorbates on the Secondary Electron Yield (SEY).

Technical Approaches:
The technical approaches are briefly outlined below. Details are avoided and have not been fully given as they are all discussed and provided in the journal papers associated with these concepts that were published in various papers spanning 2019-2022.

(A) The role of photon-processes in facilitating ionization and promoting breakdown is not new, and has been discussed in the past. For example, ionization of gas molecules by photons emitted in different parts of a discharge was shown to be a secondary ionization mechanism that produced free electrons, triggered avalanches, and governed the propagation of discharge fronts [1]. Models of photoionization in nitrogen–oxygen mixtures were reported, with the photoionization believed to occur following radiative emission by excited nitrogen molecules [1,2]; which then led to absorption-induced ionization of oxygen. Formulations were subsequently used for positive and negative streamer simulations in uniform and non-uniform electric fields [3-5]. Photoionization leading to electron creation was shown to be especially important in the propagation of positive streamers. Unlike negative streamers, electron transport in positive streamers generally cannot provide seed electrons upstream since these charges travel in a direction opposite to the streamer propagation. So in the absence of pre-ionization (such as due to previous discharge pulses or radiation from cosmic rays), photon-ionization produced by the streamer itself is the likely prevailing process responsible for creating seed electrons [6-10]. The photon processes were also hypothesized to be responsible for bringing about the streamer branching [8] and the path deviations seen experimentally [11].

Treatments of photon transport for ionization was carried out based on a particle-in-cell Monte Carlo Collision scheme with isotropic, spontaneous photon emission events [12].

To maintain a manageable computational effort, two lifetimes of 5 ns and 15 ns were associated with the excited species, and used as the basis for photon generation following atomic excitation via electronic impact. The usual random number generation technique was employed for selecting the photon emission times. Experimental various data available in the literature for excited states of nitrogen [13-15] and oxygen [13-16] show a variation and dependency on both the excited state and wavelength. For example, Musielok et al. [17] reported an average lifetime of 43.5 ns for the $3p^4D^0_{7/2}$ nitrogen state, and an average lifetime of 24.7 ns for the $3p^4S^0_{7/2}$ nitrogen state. Zheng and Wang [16] showed that the lifetimes for some excited states of atomic oxygen could range from 1.687 ns to 199.1 ns. A more complete transition rate data for atomic nitrogen and oxygen is available from a NIST publication [18]. Fierro et al. [12] used a transition rate of $2x10^8$ s^{-1}, which agrees well with our choice of a lifetime of 5 ns. The use of a 15 ns lifetime corresponding to a transition rate of $6.67x10^7$ s^{-1} accommodates the fact that some excited states have longer lifetimes. So overall, our choice of a two-lifetime model, aimed at incorporating a simple approximation that takes account of previous reports, appears reasonable.

Photons impacting an electrode with energy greater than the workfunction, were taken to produce electron emission. However, the photoemission coefficient can be expected to be much smaller than unity, since photons do not always contribute new electrons to the system. The quantum efficiency is generally below unity and a strong function of the photon energy. In the extreme case, photons at wavelength above 300 nm hardly lead to photoemission as they have energies lower than the workfunction barrier at a typical metal surface. From a purely geometrical point of view, there is the additional finite probability that emitted photons will escape from the gap depending on their initial position and emission direction. Hence, many of the emitted photons might not even impact an electrode, and would be lost. Finally, it is also likely that some of the photoelectrons created within the electrodes might suffer random collisions, and follow trajectories that do not lead them back to the surface; but instead result in their ultimate burial inside the metal following continual momentum exchanges and energy loss through inelastic collisions. In any event, the overall photoemission coefficient ($''p''$) would be expected to have a low value. Reports in the literature [19, 20] point to magnitudes below 0.5 percent. Here different values were tried, with $p \sim 0.005$ yielding reasonable results.

The standard scattering mechanisms for both elastic and inelastic collisions between electrons and the nitrogen and oxygen atoms were implemented within the Monte Carlo approach [21, 22]. Cross-sections for the various scattering processes were taken from reports by Phelps and Pitchford [23] and Itikawa et al. [24, 25]. Also, since the movement of ions is severely limited due to their large mass (relative to the electrons), the ions were treated as virtually immobile. This is especially true for the oscillating fields under the RF excitations studied here. Unlike DC discharges for which the flow of ions to the cathode may play, the breakdown behavior at the higher frequencies is controlled mainly by electron transport. Furthermore, for calculations of the breakdown threshold where one is at the verge of a self-sustained plasma, the electron and ion densities were relatively modest. Hence, for this scenario of a weakly ionized gas (i.e., $n_e << n_n$, where n_e and n_n are the free electron and neutral densities, respectively), the electron–electron, ion–ion, and electron–ion scattering were all neglected. Also, unlike microgaps where field emission due to cathode electron tunneling can modify the characteristic behavior [26, 27] or cause deviations from the Pachen law [28], such

quantum aspects were assumed to be negligible. Other approximations included neglect of three-body processes due to the low densities near the breakdown threshold [29], though reports of such treatments are available in the literature [30].

Photoionization of the gas can involve a single-photon, multiple photon absorption, or even a tunneling mechanism if the photon intensity is strong enough to change the atomic Coulomb potential [31]. The two latter options are neglected since the multi-photon scenario requires a high flux, while the tunneling possibility relies on very strong electric fields. Here a photoionization cross-section of 8 x 10^{-19} cm^2 was assumed [32], which is within the lower range reported by Stephens et al. [33]. This adjustment to a lower value, accounts for our neglect of the predissociation and quenching processes. To clarify, predissociation can result wherein the upper excited state spontaneously transitions into a lower, unbound state, resulting in molecular dissociation. Furthermore quenching, which is a pressure-dependent process of an excited state being de-excited or dissociated via a neutral–neutral collision (i.e., radiationless de-population of the excited states), can also occur. Our approach in spirit is qualitatively similar to a detailed kinetic treatment by Stephens et al. [33]. In their approach, excited states with a high predissociation fraction above 60% were neglected, which sharply reduced the number of photoionization capable transitions. Finally, though sophisticated methods based on data for frequency-dependent photoionization cross-sections $\sigma(v)$ exist [34], for our Monte Carlo implementation, a fixed interaction rate S ($=\sigma\ N_0\ c$) was used for the photons, with N_0 denoting the neutral atom density, and c the speed of light. As usual, a probabilistic time t_{ph} for a photoionization event was generated based on a random number r as: $t_{ph} = -[\mathrm{Ln}(r)]/S$. Movement past the simulation box within t_{ph} was taken to denote a photon loss.

Other aspects of our simulations included the following: (a) Inclusion of secondary electron emission (SEE) due to electron impact at the electrodes. Under the conditions of an oscillating field and high pressure (leading to significant scattering), electrons would not be expected to impinge on the electrodes with very high energies as typically required for strong secondary emission. However, for completeness, this process was included based on the Furman-Pivi model [35]. Details pertaining to the SEE model implementation by incident electrons have been discussed elsewhere [36]. (b) Potential electron emission due to the impact of ions at the electrodes was ignored, given the improbable chance that the more massive ions move much, if at all, and have a much lower likelihood to possess the high impact energies required for emission. In the RF regime, the positional oscillation amplitude of the electrons due to the applied fields is small relative to the discharge dimensions, making large energy gains or highly nonlinear transport quite unlikely. (c) High-energy ion-neutral collisions can also be ignored under these RF excitation conditions. Besides, ion densities are anyway low at or below the breakdown threshold. (d) As regards photons, photoemission from the electrodes was considered based on a probabilistic approach. Random numbers r_i were generated, and photoemission allowed only for cases when random numbers were lower than the photoemission coefficient (i.e., $r_i < p$). The emitted electrons were characterized by a thermalized semi-hemispherical distribution in velocity space. Photons not incident on the electrodes were assumed to be lost from the system boundary. (e) A one-dimensional Poisson solver was also included for self-consistency.

The simulation results for ionization and possible charge growth leading to breakdown were compared to experimental data generated within our group. Briefly, RF breakdown data was obtained across an airgap with 10 cm diameter Bruce electrodes in atmospheric

air at mm gap distances. An LC tank was resonantly excited with a 50 Ohm RF-source, ~1 kW output, to produce the high voltage amplitudes necessary to breakdown mm to cm gaps. Adjusting rise times and power levels, the system allowed for the study of RF breakdown under various conditions and high electric fields. A schematic of the experimental set up is shown in Figure 1, with details given elsewhere [37]. The large electrode areal size of the Bruce electrodes relative to the airgap is evident. Since the electrode diameter was much larger than the gap distances, most of the photons created during high field stressing within the gas are likely collected at the one or the other electrode, and comparably few photons would escape the system. Hence, this structure affords the assessment of possible photon-assisted processes in creating and sustaining charge densities during RF operation.

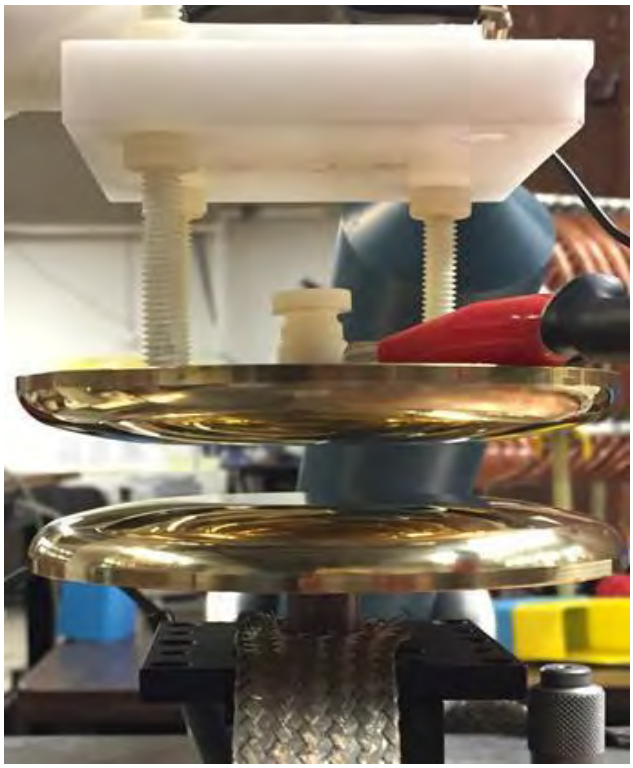

Figure 1. Experimental setup for RF breakdown measurements showing the geometry and areal size relative to the airgap of the Bruce electrodes.

(B) Study of electron emission was based on the Fowler-Nordheim process, which depends on three factors: Electron emission depends on three factors: (i) the tunneling probability, that is influenced by details of the electronic wavefunction in the presence of the local potentials, (ii) the work function barrier (Φ_B) at the boundary that is dependent on material details such as the crystal orientation, the presence of possible defects, etc., and (iii) the density of states (DOS) at the metal surface that influences the supply of electrons. These various factors can collectively be evaluated based on Density Functional Theory (DFT). Such analysis also yields internal potential profiles, from which the electron wavefunctions (and hence the electron density) can be obtained through a solution of the one-dimensional Schrödinger equation if atomic details parallel to the surface are ignored.

In order to obtain the parameters (such as work functions, total density of states, and frequency- and wavevector-dependent permittivities) necessary for modeling the electron emission, density functional theory calculations were carried out based on the Vienna Ab initio Simulation Package (VASP) [38]. It is a first-principles density functional pseudopotential software tool. The plane wave kinetic energy cutoff was set to 600eV with the *k*-point integration being done by a modified tetrahedron method for total density of states calculations [39–42]. The DFT scheme utilized the generalize gradient approximation (GGA) to the exchange-correlation potential, as parameterized by Perdew–Burke–Ernzerhof [43]. The calculations for the emitting surface consisted of crystal made up of 10 host atom periodic supercells, with a *k*-point sampling of a 10 × 10 × 2 Monkhorst Pack mesh [44]. For all surface calculations, a calculated bulk equilibrium lattice constant was obtained, and seen to be in excellent agreement with the experimentally reported values.

(C) Electric fields that electron emission at the cathodes were computed on the basis of the Linear Charge Model (LCM) [45]. The advantage of the LCM, and similar models [46-48] is that they facilitate the study of key array parameters, such as emitter height, tip radius, and array geometry, while invoking conceptual simplicity. These models yield quick solutions to the potentials and electric field distributions for an array of varying emitter heights and are designed to provide an equivalent structure consisting of a line charge and its image, to replace the actual nanoprotrusion. Simple analytic expressions are then made available, instead of having to solve a three-dimensional problem with the affiliated boundary conditions [49]. For an i^{th} emitter subjected to a uniform external field of magnitude F_0 along the z-axis, the potential $V(r,z)$ is given by [45, 50]:

$$V(r,z) = \sum_i \frac{\lambda_i q F_i(r,z)}{4\pi\epsilon_0} - F_0 z \quad , \qquad (1a)$$

$$\text{where, } F_i(r,z) = \int_{-L}^{L} \frac{s}{\sqrt{r^2+(z-s)^2}}\, ds \quad , \qquad (1b)$$

$$\text{and, } \lambda_i = \frac{4\pi\epsilon_0 F_0 z_i}{\left[z_i \ln\left(\frac{L_i+z_i}{-L_i+z_i}\right) - 2L_i\right] q} \quad . \qquad (1c)$$

In the above expressions, *"L_i"* represents the half-length of the line charge associated with the i^{th} emitter, *"z_i"* is the height of the zero-potential surface at the location of the line charge, *"q"* the elementary charge, and *"ε_0"* the permittivity of free space. Based on the above formulation, the static electric fields and potential distribution from an array of emitters of any specified height can be obtained.

(D) Calculations of wavefunctions[$\psi(z)$] are important for obtaining the tunneling probability that helps yield the emission current. In addition to $\psi(z)$, the electrode work function (Φ_B) is another parameter that dictates emission and needs to be carefully calculated. The workfunction value essentially signifies the energy needed to pull an electron from inside the material and place it in a quasi-free state at the vacuum level.

However, the Φ_B value can be altered due to surface modifications. The details of the Work Function were obtained from the DFT analysis described briefly in section (A) above. For simplicity, a one-dimensional model was used to evaluate the internal potential V(x) from DFT calculations. This internal potential V(x) was then used to

determine the electronic wavefunctions $\psi(x)$ from a solution of the Schrodinger Wave Equation (SWE). This equation is:

$$- [\hbar^2/(2m)]\, d^2\psi(x)/d^2x \; + \; V(x)\, \psi(x) \; = \; E\, \psi(x) \; . \qquad (2)$$

where $\hbar$ = reduced Planck's constant, $\psi(x)$ denotes the electron wavefunction, $V(x)$ is the internal potential obtained from DFT calculations, and E the energy of an electron in the metal. The above equation was solved using the Numerov discretization technique [51]. Very briefly, the entire simulation volume consisting of the metal, the interface, and the outer vacuum was divided into three sub-regions: (i) an interior bulk-like zone A with $x < -x_1$, (ii) a zone B in the metal but next to the interface, $-x_1 < x < x_2$, and (iii) the vacuum zone C for $x_2 < x$.

The wavefunctions $\psi(x)$ for the three zones can be written as:

(i) **Zone #A:**

$$\Psi_A(x) \; = \; exp[i\, k_x\, x] + R\, exp[-i\, k_x\, x] \, , \qquad (3a)$$

where ″R″ denotes a refection coefficient,

(ii) **Zone #B:** $-x_1 \leq x \leq x_2$, where $\Psi_B(x)$ obeys the Numerov relation:

$$\Psi_B(x+dx) = \{2[1-(5/12)h^2k^2(x)]\; \Psi_B(x)-[1+(1/12)h^2k^2(x-h)]\Psi_B(x-dx)\}/\{1+(1/12)h^2k^2(x+h)\}, \qquad (3b)$$

Where:
$k^2(x) = (2m/\hbar^2)[E - V(x)]$; $k^2(x+h) = (2m/\hbar^2)[E-V(x+h)]$; $k^2(x-h) = (2m/\hbar^2)\,[E - V(x-h)]$.
In the above, ″$\hbar$″ while ″h″ denotes the spacing between adjacent grid points.

(iii) **Zone #C:** $x_2 \leq x$, where $\Psi_C(x)$ obeys the relation:

$$\Psi_C(x) = T\, exp[ik_x\, x]\, [Ai(-\eta_0) - i\, Bi(-\eta_0)] \; , \qquad (3c)$$

where $\eta_0 \; = \; [(E - E_F - W)/(qF_0) + x]\, \{2qm\, F_0 / \hbar^2\}^{1/3}$, and $k_x^2 \; = \; (2m/\hbar^2)\, [E - V_C(x)]$.

The total current density ″J″ is given by:

$$J \; = \; [\hbar/(2mi)]\, [\psi^*\, \delta\psi/\delta x - \psi\, \delta\psi^*/\delta x] \quad . \qquad (3d)$$

With ″N″ discrete points chosen in Zone #B, one can obtain ″N-2″ equations of the form similar to equation (3b):

$$\Psi_{B,i+2} = \{2[1-(5/12)h^2k_{B,i+1}^2]\Psi_{B,i+1} - [1+(1/12)h^2k_{Bi}^2]\; \Psi_{Bi}\}/\{1+(1/12)h^2k_{B,i+2}^2\} \; , \quad 1 < i < N-2 \qquad (3e)$$

In addition, there would be 4 equations rising from the 2 boundary conditions each at the left and right boundaries. Thus, a total of $N+2$ equations for the $N+2$ unknowns (Ψ_{B1} , Ψ_{B2} ,.... Ψ_{BN} , R and T) which can all be obtained self-consistently. The transmitted current density then works out to:

$$J=[\hbar/(2mi)]\; \{[\psi_{BN}^*][1/(2h)][3\Psi_{BN} - 4\Psi_{BN-1}+\Psi_{BN-2}\,] - \psi_{BN}[1/(2h)]\; [3\Psi_{BN}^*-4\Psi_{BN-1}^*+\Psi_{BN-2}^*]\}. \qquad (4)$$

(E) Electron transport was modelled based on the kinetic particle-in-cell scheme [52-54]. Since high emission current densities are of paramount importance to high power applications, one needs to carefully account for carrier-carrier scattering that could contribute to both pulse distortion and local field modifications due to space charge. The short-range part of the Coulomb interaction has typically been accounted for by considering an additional *k*-space scattering mechanism in Monte Carlo transport procedures [55]. However, many-body contributions to scattering [56] are then ignored. Also, the *k*-space treatments of such interactions regard the events as being localized and instantaneous, even though in reality the process unfolds in an extended manner over space and time [57]. With regards to the Poisson equation, needed for obtaining the local driving electric fields, the solution should ideally be obtained on a mesh, whose size is smaller than the extrinsic Debye length [58]. However, such an approach would require a large number of node points, and would present a numerical bottleneck.

The combination of direct and mesh forces has been studied in the past, starting with the particle-particle-particle-mesh (P^3M) algorithm proposed by Hockney [59]. Extensions and alternatives to the method gradually emerged based on a corrected-Coulomb (or hybrid) approach [60, 61]. While these algorithms represent a large improvement, they tend to work well when the required precision is relatively low, and the particles are distributed more or less uniformly. However, for higher precision, the computational times can become prohibitive. The Fast Multipole Method (FMM) originally devised by Rokhlin [22] as a fast solution method for the Laplace equation, and refined by Greengard [63], is perhaps a better option. The FMM uses multipole moments to represent distant particle groups and introduces a local expansion to evaluate the contribution from distant particles in the form of a series. In any case, given the computational speed of the FMM, its accuracy, and treatment of both the Poisson and carrier-carrier interactions, this scheme was used. Specifically, the FMM library from the Scalable Fast Coulomb Solver (ScaFaCoS) package [64] was chosen, as it has a best-case O(N) complexity for *N*-body problems [65].

(F) Hydrogen transport in copper and carbon fiber materials was treated and analyzed based on the molecular dynamics (MD) technique. The first step involved the construction and synthesis of the material structure, including the periodic lattice. For copper, the face centered cubic (fcc) lattice is the appropriate structure. An atomic-level approach using the LAMMPS software tool that included atomic bonding was used [66]. For the carbon fibers , the initial step involves the interconnection of an array of graphene sheets resembling ladder like structures that can structurally self-organize.

The choice of ladder-like monomers used as the structural units of the overall carbon fiber structure was based on previous studies which have reported similar intermediate structures during the manufacturing [67] of real carbon fibers (CFs). This system packed with monomers was initially relaxed and thermalized at 300 K using the many-body MD technique. This entailed letting all the constituent atoms within the structure move dynamically with each subjected to the many-body forces from all the remaining atoms in the ensemble. Standard Newtonian mechanics were applied. Next, the well relaxed monomers in the simulation cell were connected with each other to build the CFs. The newly created bonds were then relaxed at their equilibrium bond length using the stepwise bond relaxation method [68]. Following bond creation, angles and dihedrals

were added and the system was again relaxed. At the end of this step, the density of the CF ensemble was checked for verity. In our simulations, a density value of 1.86 gm/cc was obtained for the CF system at the end of these processes, which falls within the standard range of 1.75 gm.cc–1.93 gm/cc [69] reported in the literature for carbon fibers. Our simulated structure had approximately 51,000 particles. In our study, hydrogen atoms were subsequently placed within the carbon fiber matrix, and their motion followed based on Newtonian dynamics as with the usual MD procedure. The goals of the calculations were two-fold. First, obtain quantitative predictions of the diffusion coefficients as a function of temperature for hydrogen within the copper and carbon fiber materials. Since localized heating is expected to be a natural outcome during the operation of high power HPM devices, carrying out the calculation at different temperatures provides a more meaningful and relevant exercise for outgassing predictions. Second, obtain the time-dependent outgassing dynamics characterized by a simple outflow time constant.

(G) Finally, an important question that was addressed based on fundamental physics and materials science was the role of absorbates on the Secondary Electron Yield (SEY). First-principles calculations coupled with Monte Carlo simulations are used to probe the role of a surface CO monolayer formation on secondary electron emission (SEE) from Cu, Ag, and Au (110) materials. It is shown that formation of such a layer increases both the secondary electron emission in all systems. Analysis of calculated total density of states (TDOS) in Cu, Ag, and Au, and partial density of states (PDOS) of C and O confirm the formation of a covalent type bonding between C and O atoms. It is shown that such a bond modifies the TDOS and extended it to lower energies, which is then responsible for an increase in the probability density of secondary electron generation. Furthermore, a reduction in inelastic mean free path is predicted for all systems. Our predicted results for the secondary electron yield (SEY) compare very favorably with experimental data in all three materials, and exhibit increases in SEY. This is seen to occur despite increases in the work function for Cu, Ag, and Au. The present analysis can be extended to other absorbates and gas atoms at the surface, and such analyses will be present elsewhere.

It is well known that the presence of the surface contaminants can increase or decrease the SEY significantly [70]. For example, as received samples of Cu, Ag, and Au that are not subjected to cleaning or any artificial treatment have SEY of about 200% [71-73], while the values obtained from the corresponding cleaned sample surfaces have been found to be much lower at around 150% [71-73]. Since materials are exposed to atmosphere, surface contaminants could include water, carbon compounds, oxygen, nitrogen, and argon. Among all the contaminants, C and O have been reported to be present at the highest concentrations [71]. Furthermore, in numerous reports, removal of C and O from the samples has been seen to significantly reduce the SEY of the processed system [71-72]. The extent of C or O if present at surfaces, would likely be very small (e.g., a few monolayers in extent at best), and insignificantly smaller than the electronic mean free paths. Hence, their influence on electron scattering or energy loss over the surface regions can be expected to be inconsequential in affecting the overall SEY characteristics. It is far more likely that their chemical interaction with the host material may be leading to changes in the workfunction, or local density of states, or bonding strengths that could then be the reason for observed SEY shifts If so, surface processing would certainly affect SEE.

The aim of this part of the project work, was to use appropriate simulations to investigate the inherent physics and disentangle the role of each chemical surface component in influencing the SEY values. The analysis has been applied here for copper, gold and silver materials, though the method is general and would allow the investigation of other emitter materials and/or surface absorbates as well. While copper might have been sufficient for a numerical study, Au and Ag were additionally included here for a broader evaluation as these elements all belong to the same IUPAC group. The role of surface conditioning and the presence of the C and O contaminants is clarified. In the process, possible routes for developing inherently low-SEE emitters can then naturally emerge, though extensions to other materials and contaminants will be discussed elsewhere.

While existing literature on the relation between surface composition and SEY is substantial, much of it has been experimental or based on macroscopic or empirical analysis. Studies of a more fundamental nature, from electronic structure point of view, are relatively scarce. Furthermore, the role of the surface and any absorbates that may be present, has been ignored in most considerations and analyses. It is important to fill this gap in knowledge, as it will lead to a deeper understanding and better control over SEE, especially since the physics at the surface and the surrounding monolayers dictates the eventual outcomes. For instance, absorbates could alter the work function [74-77], produce three-dimensional variations in density of states to affect the inherent source function, possibly cause lateral WF variations [78-80].

Studying the formation of CO monolayer and its effect on physical properties like work function, inelastic mean free path, and secondary electronic emission were studied. To better understand the general role of CO, we studied its formation in several systems (Cu, Ag, and Au) where experimental data is available for comparison. The studies presented here are carried out based on a combined first principles and Monte Carlo method. The results of first principles calculation of parameters such as the work functions, total density of states, frequency- and wavevector-dependent permitivities are necessary for obtaining the inelastic mean free path (IMFP), stopping power (SP), and SEY values based on Penn's theory [81]. The electron emission process itself is simulated by including the associated transport, inherent scattering and exchanges of energy and momentum within the target, with eventual escape of electrons over the work function barrier at the surface. Monte Carlo simulations are used to model electron transport, taking account of elastic scattering based on the Mott theory, and inelastic collisions based on energy-dependent energy loss function and mean free paths [82, 83]. The present MC scheme naturally builds in cascade effects associated with secondary and tertiary electron generation.

Significant Results and Findings:
The summary of the main results from the research for the 2019-2022 duration are given below.

(i) In order to determine gas breakdown, the variations of electron concentrations over time were probed through Monte Carlo simulations. Net time-dependent growth in electron density indicates a scenario wherein one is past the breakdown point. Similarly, at around the breakdown threshold, the net density increases would be balanced by electron losses at the surfaces and through attachment. Using the above as a measure to assess breakdown, Monte Carlo simulations were performed starting with 50 seed electrons released from the cathode. Representative results for the evolutionary time-dependent population obtained from the numerical calculations are given in figure 2(a)-2(c) for a 5 mm air gap. Three different

electric field magnitudes E_0 of 36 kV/cm, 37 kV/cm and 37.8 kV/cm, respectively, were used, with the time-dependent driving field $E(t)$ taken to be $E_0 \cos(\omega t)$. A 3.3 MHz excitation frequency was used for all three cases, and the temporal evolution of the electron populations obtained. The photoemission process was explicitly included. In all three cases, the electrons were initially released from the cathode (assumed to be at $z=0$, with the anode plane situated at $z=L$), with a thermalized semi-hemispherical velocity distribution. The time period (T) for the 3.3 MHz excitation is ~303 ns, and so the electric field flips polarity after around $T/4$ (= 75.75 ns). In Figs. 2(a)-2(c), during the initial times, electrons gain energy as they are accelerated by the field towards the anode. The average electron transit time to the anode at the fields chosen, based on the drift velocities reported in the literature [84], is about 25 ns. During traversal, electrons excite neutral gas atoms along the way, though the bulk of the excited atom population has a spatial distribution (not shown) that is *asymmetrically shifted towards the anode*. The space close to the emitting cathode is a virtual ″dead zone″, since electrons need to first be accelerated to energies above the excitation thresholds before any atomic excitations can be enabled. Due to the ″dead zone″, since more excited atoms lie on the anode side, the photon emission sites would also reflect an asymmetric distribution. As a result, following isotropic emission, the photons would be more likely to hit the anode (which would be closer and present a larger solid angle), in comparison to the cathode. The resulting photo-emitted electrons from the anode, however, due to the electric field direction, would likely be pulled back and re-absorbed. Only the weaker and less frequent photon-emission processes at the cathode would successfully inject carriers into the system. However, given the distribution of emission times (about the two chosen lifetimes in this case), photon emissions occurring later in time, on the other hand, would contribute to charge growth from the electrode at $z=L$ since the polarity reversal at the closer electrode would then begin to support sustained injection.

The slight (almost imperceptible) dip in population seen to occur around 25 ns in Figures 2(a)-2(c) is due to the collection of the faster electrons at the anode from among the ensemble. Though electron collection continues, charge creation in the system through impact ionization and photoemission enables a continued population increase until about 75 ns. Field reversal beyond this time, slows down electrons, and diminishes the rate of atomic excitation and ionization. However, since the electron velocities do not change instantaneously, the losses at the electrode (at $z=L$) continue. The net effect is a continuous reduction in the free electron population which is predicted to fall to zero for all three electric fields in Figures 2(a)-2(c). However, electrons continue to be generated through photoemission arising from the random (discrete event) radiative decay of excited neutral atoms. The population is predicted to build up after 250 ns. It may be mentioned that the emission times of the photons follows a decaying exponential distribution in time, with a mean equal to the chosen lifetime. The distribution of emission times, implemented on the basis of the usual random number generation.

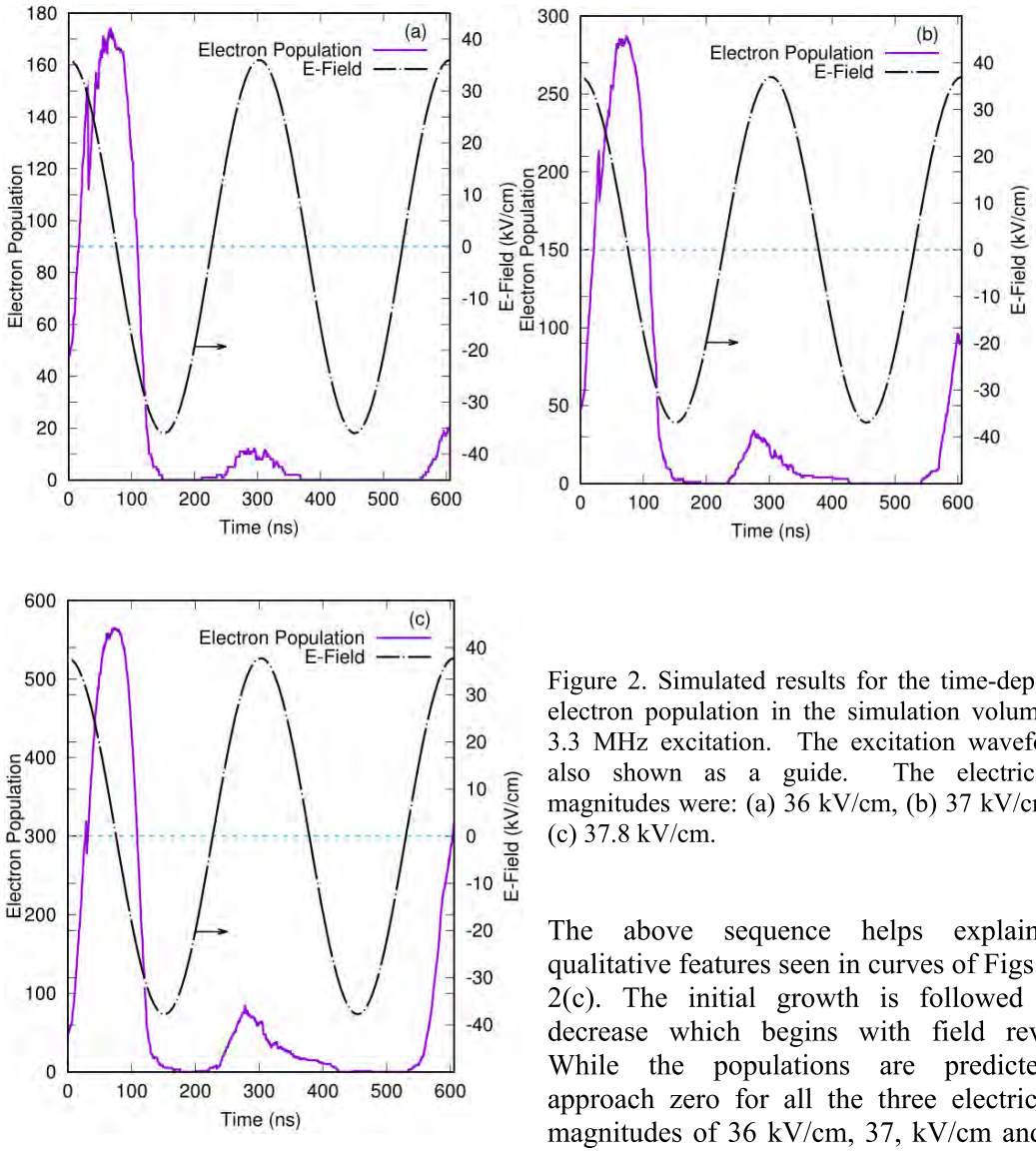

Figure 2. Simulated results for the time-dependent electron population in the simulation volume at a 3.3 MHz excitation. The excitation waveform is also shown as a guide. The electric field magnitudes were: (a) 36 kV/cm, (b) 37 kV/cm, and (c) 37.8 kV/cm.

The above sequence helps explain the qualitative features seen in curves of Figs. 2(a)-2(c). The initial growth is followed by a decrease which begins with field reversal. While the populations are predicted to approach zero for all the three electric field magnitudes of 36 kV/cm, 37, kV/cm and 37.8 kV/cm, continued sporadic photon emission at later times after the electric field has regained its original polarity past ~227 ns, fuels a re-growth. The values are higher with increasing electric field. For example, at the 37 kV/cm and 37.8 kV/cm, the simulations predict the net electron population at the end of the time-scale shown *to be larger than the starting value of 50*. In the present analysis, numerous simulations were run to probe this growth given the statistical nature of the Monte Carlo analysis. In each case, the breakdown field was chosen from these simulations as the minimum field value for which a sustained electron population was obtained over time after multiple cycles. The number of electrons at the end of multiple cycles had to exceed the starting population.

An important objective was to assess the contributory role of photon-assisted processes on the overall RF breakdown of air at atmospheric pressures. Towards this goal, simulations were carried out to: (i) Probe possible differences between predictions with and without inclusion of photon mechanisms. The photon mechanisms here encompass photo-ionization of bulk gas, and photo-emission from the electrodes. (ii) Evaluation of the role of photo-ionization, relative to and separate

from the photo-emission contribution. The qualitative essence from our results appears to be that in the absence of any photon-processes, the populations at a given applied field strength would likely not be revived through re-generation. Thus, a much higher breakdown field would be required to breakdown achieve. Furthermore, even with inclusion of photo-ionization, the free electron population though longer lived with some re-generative features, could eventually decay at a given voltage. However, with photo-emission also present, breakdown could be achieved at the same voltage. As a demonstration, results for the time-dependent electron population at a 3.3 MHz excitation obtained at an electric field magnitude of 39.5 kV/cm, are shown in Figure 3. Without any photon processes, the predicted time evolution of the electron density, starting from the same 50 seed electrons initially, is predicted to have an early large and rapid growth, leading to a population of almost 1,200 electrons within about 25 ns. This is seen to be followed by a precipitous decay to zero values, in Figure 3. That is, the initial electrons are swiftly swept out from the gap without secondary emission production from photon processes. By contrast, in the previous case (shown in Fig. 2) with the inclusion of photon processes, a RF field magnitude of 37.8 kV/cm was shown to be sufficient for the system to be at the breakdown threshold. With inclusion of only photo-ionization, the curve in Figure 3 exhibits partial sustainment after about 26 ns. Nonetheless, the population cannot be sustained for longer times and eventually decays completely. A second difference between the results of Figures 2 and 3, is the associated temporal scale. While the populations are predicted to remain above zero until at least 150 ns, and recovering to fairly robust values beyond 550 ns with the inclusion of photon processes in Figs. 2(b) and 2(c), the result of Figure 3 shows a quick decay over a ~25 ns timeframe without photon processes, and extinction after ~ 300 ns with only photoionization included. It is thus clear that photoemission is the more dominant photon process under the conditions investigated.

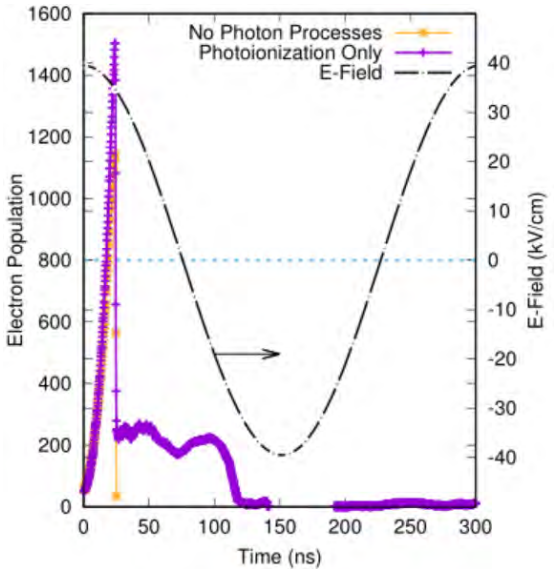

Figure 3. Comparative simulation result of the time-dependent electron population for a 3.3 MHz excitation in the absence of any photon processes, and with the inclusion of just photoionization. Electric field magnitude of 39.5 kV/cm was chosen.

The above simulation results were then used as the basis for calculating the breakdown field versus air-gap length at atmospheric pressure for the 3.3 MHz

excitation. The simulation results were compared with experimental data obtained within our group. The results are shown in Figure 4. Given the statistical nature of the Monte Carlo scheme, at least a couple of simulations with different random number seeds were carried out at each gap length to ensure that a self-sustained and repetitive electron population could be achieved at each applied field. Not much difference was seen in the outcome, a result in keeping with the report by Krile and Neuber where the seed electrons had been varied [85]. Gap lengths varying from 1.5 mm to 5 mm were used for purposes of modeling. The simulation results were compared with experimental data obtained for two cases, one with and the other without ultraviolet (UV) illumination of the gap. In the UV illumination case, a 100 microsecond pulsed UV lamp (wavelength as low as 180 nm) was utilized to provide seed charge carriers for the breakdown via photoemission form the electrodes. Alternatively, a UV LED at 265 nm was utilized which provided similar results, albeit at much lower output power (~5 mW). Simply relying on natural charge carrier density is known to increase breakdown delay and fluctuation amplitudes as was observed here. Since the simulation assumes freely available electrons at simulation start, it is expected that the simulation should more closely track the UV case, which it does, cf. Figure 4. Again, due to the statistical delay for the appearance of initiating free electrons and owing to the fast voltage ramp that is thus allowed to climb for a longer time, without UV, the measured breakdown fields are much higher.

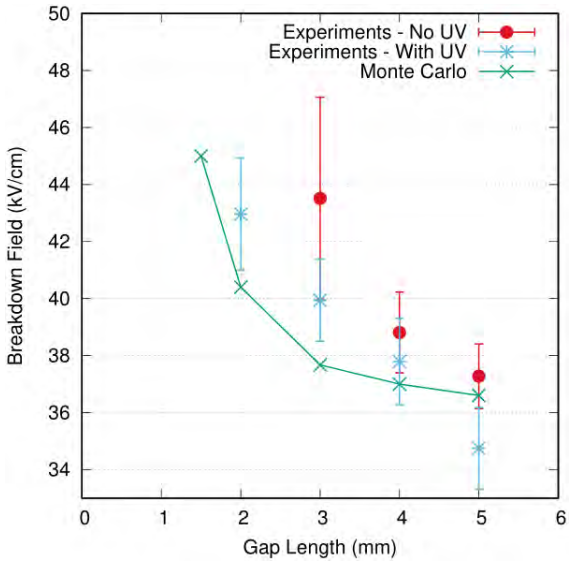

Figure 4. Results for the breakdown field versus air-gap length at atmospheric pressure, and a 3.3 MHz excitation frequency. The simulation results were compared with an experimental data point obtained for a 5 mm gap.

Regarding the gap distance, a monotonic decrease in breakdown field is predicted from a value of about 45 kV/cm for the 1.5 mm gap, down to roughly 36.8 kV/cm for the 5 mm case. The decrease in electric field with increasing gap distance arises from the larger transit space and time available for electrons to gain energy in either causing excitations or ionizations. Since electrons require a minimum threshold to initiate an inelastic collision, some initial space and time are wasted in building up the requisite energy. This constitutes an effective ″dead-zone″. A longer gap affords a lower fractional dead-zone, making it easier to generate and sustain charge in larger gaps, thus decreasing the driving field needed for breakdown.

The data shown here was obtained for stainless steel electrodes where the choice of electrode material yielded the most robust and repeatable results [86]. It is also possible that some electrode deterioration of the electrode might cause slight differences in the measured values. For example, though not shown, slight differences with the use of other electrode materials such as brass or aluminum were seen experimentally. This strongly suggests that the breakdown physics is likely influenced by: (a) the material workfunction, since it plays a role in the successful escape of secondary electron emission at the surface, (b) potential erosion or degradation of the surface which could alter both the local workfunction, the surface electric fields, and the material permittivity which controls the inelastic scattering [87]. These alterations could then influence field emission. A time-dependent response can also possibly emerge, and such studies will be reported elsewhere. (c) The possibility of differences in the degree of oxidation and the thickness of such overlayers. As reported about 50 years ago, the presence of oxide layers can affect and decrease the photoemission coefficient [88].

Finally, the frequency-dependent behavior for two gap lengths of 5 mm and 7 mm were obtained and are shown in Fig. 5. Roughly, a U-shaped curve is seen to results and is in line with qualitative expectations. The minimum corresponds to the situation where electrons continue to oscillate rapidly. At the high frequencies, it becomes harder for the electrons to gain sufficient energy from the field to ionize or cause as many atomic excitations. Hence, larger electric fields are needed to drive the electrons past the ionization threshold energy, and hence, higher breakdown fields are required. Lowering the frequency, on the other hand, impacts the physics in two ways. First, since the electrons do not oscillate quite as much, more are lost to the electrodes. Secondly, the delicate timing for photon-assisted charge creation is perturbed. The electric field amplitudes are below the field amplitude necessary for electron impact ionization, for longer periods. Hence, photons emitted during this "dead time" are lost. Predictions of Figure 5 show that the larger gap would require a lower field for achieving breakdown. This is again in keeping with concept of a smaller fractional dead-zone at longer gaps. Alternatively, for longer gaps, electrons are less likely to reach either boundary within a given frequency cycle, thus decreasing the loss term and needing lower fields to keep the electron populations replenished. For similar reasons, the field values for the RF case are lower than those predicted for Paschen breakdown under DC conditions of around 40-100 kV/cm [89] for gaps in this 2-5 mm range. Finally, the slow merging of the curves at the 5 mm and 7 mm gaps at high frequencies is simply the result of the loss processes at the electrodes becoming virtually negligible.

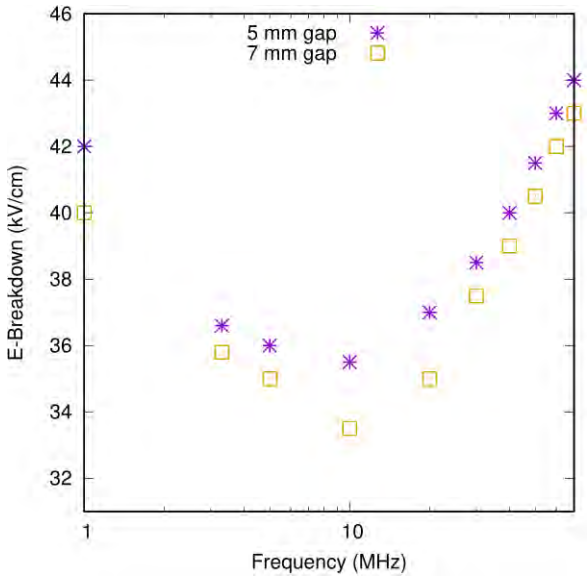

Figure 5. Predicted results for the breakdown field versus excitation frequency obtained from the Monte Carlo simulations for two different air gap lengths of 5 mm and 7 mm.

(ii) Results for temperature-dependent diffusion coefficients for hydrogen in pure copper and in the presence of a discrete set of vacancies, are shown in Figure 6. The diffusion coefficient was obtained from the slope of the mean square displacement versus time. For comparison, data reported previous by various groups [90-92] are also shown in Figure 6 for ideal copper. A fairly good agreement between data and the calculations is evident. An Arrhenius type behavior naturally emerged from the calculations for pure copper, with an activation energy of 0.43 eV and a pre-exponential factor of 2.1×10^{-7} m^2/s.

In case of vacancies, the copper system shows lower diffusion. The vacancy sites serve as trapping centers. *From the standpoint of mitigating out-gassing, the presence of discrete vacancies would then be a desirable objective.* The physics behind the vacancy trapping of hydrogen can be qualitatively explained in the following manner. Hydrogen has slightly higher electronegativity (Pauling value ~2.2) compared to copper (Pauling value of ~1.9). Hence, a hydrogen atom in a copper lattice would have a slightly negative charge, while the copper in the neighborhood would be somewhat positive. In a perfect lattice, a hydrogen atom at any site, would on average experience symmetric forces from the surrounding copper atoms. However, if the hydrogen were to approach a vacancy, there would be no positive charge around the vacancy, resulting in an asymmetric net force that would pull it away or impede its motion towards the vacancy. This is reflected in the "energy barrier" of Figure 7 as a hydrogen atom approaches a vacancy. Once in the energy well with lower energy, the hydrogen would effectively be "trapped". The process can alternatively be thought to

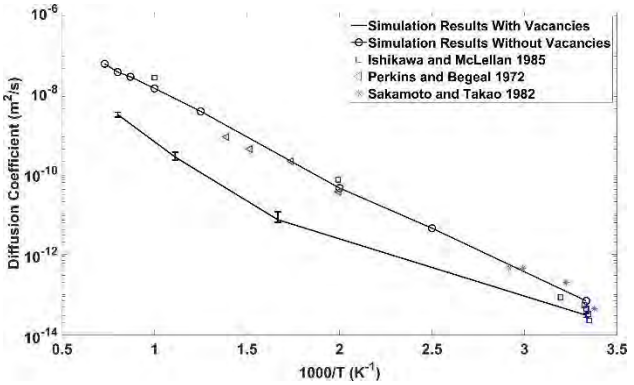

Figure 6. Comparison between the temperature dependent diffusion coefficients for hydrogen in copper obtained from the simulations, and various data points reported in the literature.

arise from reductions in charge density in the vicinity of a vacancy that provide an iso-surface for collective hydrogen binding and segregation [93].

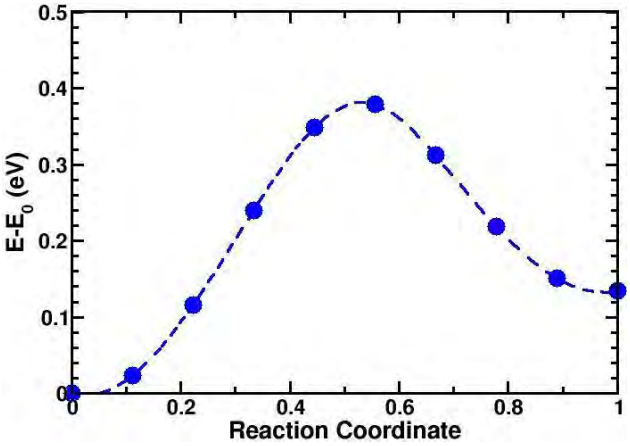

Figure 7. The diffusion energy barrier of a directional hydrogen displacement in the vicinity of a vacancy [with relative coordinate of (½, ½, ½)] in a copper lattice obtained from DFT calculations. A finite barrier to detrapping with a secondary local minima away from the vacancy (reaction coordinate=1) is evident.

The temperature-dependent diffusion coefficients *D* obtained from the MD simulations for copper and the carbon fiber structure are shown in Figure 8. For copper, the data shown previously in Figure 6 is also shown for comparison. An Arrhenius type behavior with $D(T) = D_0 \exp[-E_a/(k_B T)]$ naturally emerged from the calculations, with an activation energies of 0.45 eV and 0.386 eV for copper and carbon fiber, respectively, and the corresponding pre-exponential factors of 2.34×10^{-6} m^2/s and 1.251×10^{-8} m^2/s. From Fig. 8, it is evident that the diffusion of hydrogen in carbon fibers is lower than that in copper by about a factor of 15.5 at 400K, and a factor of 86.8 at 1000 K. *Thus, the relative benefits of using CFs over copper for reduced outgassing are enhanced at higher temperatures. In the context of high power devices, where heating is expected, there would be greater utility in CF electrodes over traditional copper material.*

In order to gauge the reflection and absorption of hydrogen incident onto the copper surface, which effectively is the inverse of the outgassing process, simulations were performed at

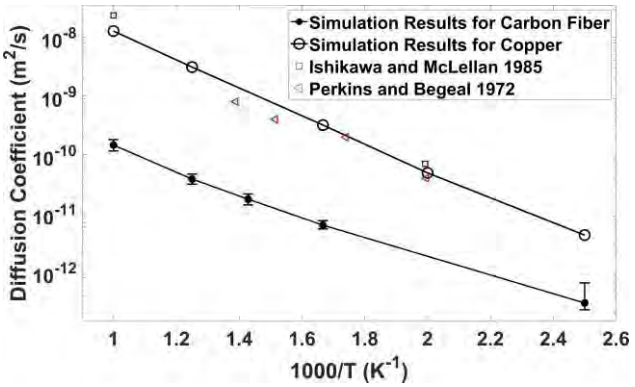

Figure 8. Comparison between the temperature dependent diffusion coefficients for hydrogen in copper and carbon fiber. Some reported data for copper is also shown for comparison.

different energies and angles. At each energy 5-7 separate simulation sets were carried out to obtain better statistics. For each simulation case, 10 entities were projected onto the copper at definite time intervals. Also, to avoid any lattice distortion, the atomic system was continually thermalized after each run to eliminate any memory effects. The number of reflections were counted, and the mean (as well as standard deviation) over all simulations for given energy were obtained. Results for normal incidence are shown in Figure 9. Temperature of the copper was taken to be 800K. The main feature is that at low incident energy, ability to bounce back easily is low. This leads to low reflection coefficients. At high energies, the atoms are mainly transmitted through, again leading to a lower reflection. Hence, a local maxima in the reflection curve is predicted in Figure 9. For practical convenience, a curve fit to the data was obtained, and is given as:

$$R(E) = -1.674\times10^{-2}[Log_{10}(E)]^7 + 2.284\times10^{-2}[Log_{10}(E)]^6 + 1.092\times10^{-1}[Log_{10}(E)]^5 - 1.221\times10^{-1}[Log_{10}(E)]^4 - 2.162\times10^{-1}[Log_{10}(E)]^3 + 6.442\times10^{-2}[Log_{10}(E)]^2 + 1.86\times10^{-1}[Log_{10}(E)] + 0.6804 . \quad (5)$$

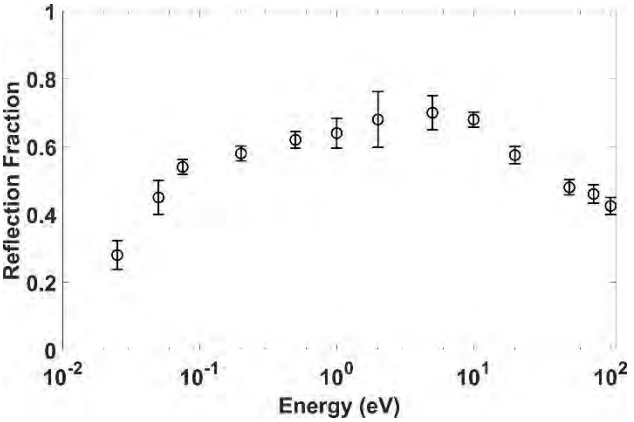

Figure 9. Energy-dependent reflection coefficient at normal incidence of hydrogen impinging on the surface of a copper electrode, calculated from Molecular Dynamics simulations.

Results at an incident angle of 30-degrees for incoming hydrogen are given in Figure 10. The overall characteristics are similar to those for the normal incidence with a local maxima. A slightly higher reflection at 30-degrees is predicted compared to the 0-degree incidence, and is associated with the shallower impact. The simulations yielded adsorption and absorption data which is presented in Figure 10 for normal incidence. As evident from the figure, adsorption is predicted to occur for incident energies below 10

eV, while absorption would dominate above 10 eV. The overall plot of Figure 11 exhibits a minima in energy which is in keeping with trends shown by Kaufmann et al. [94] for copper surfaces, and by Maya for deuterium incident on tungsten [95]. Results were also obtained for a 60-degree incident angle, and MD simulations were also carried out at a higher temperature of 1200 K. However, the results were very similar to those discussed in Figures 9 through 11, and so have not been shown for brevity. Finally, it is likely that the presence of grain boundaries, dislocations or surface adsorbates could change the energy-dependent sticking coefficients, but it is beyond the present scope.

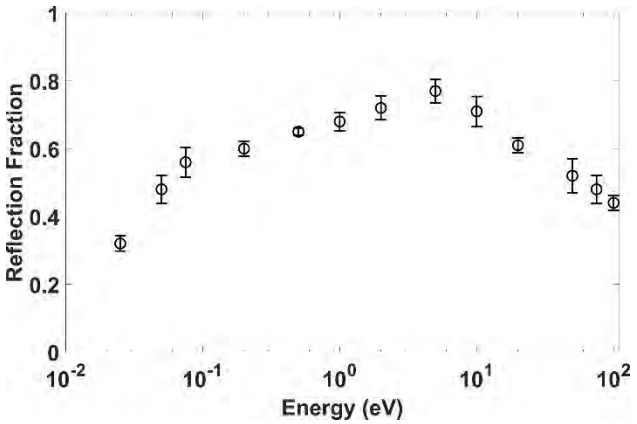

Figure 10. MD results for the energy-dependent reflection coefficient incident at a 30-degree angle on the surface of a copper electrode.

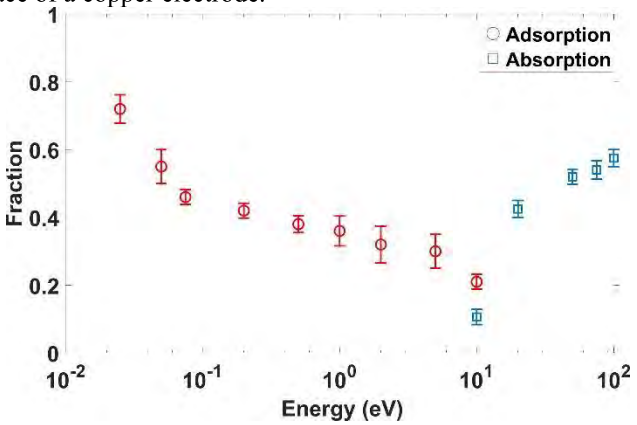

Figure 11. Molecular Dynamics calculations of energy-dependent adsorption and absorption of hydrogen at normal incidence on the surface of a copper electrode.

The above calculations and results could form the basis for predictive analysis of gas emissions for comprehensively modeling the electrical response and overall plasma behavior in pulsed power devices. The net temperature-dependent gas emission rates could be used to account for pressure changes, dynamically alter scattering rates in particle-on-cell (PIC) simulations, and probe contributions to plasma growth and field distortions. Currently for example, PIC simulations assume *some constant level of background gas*, while ignoring gas release rates, or the possible local inhomogeneities in the concentration due to outgassing. However, evaluations of the system efficiency and its space-charge could change if more realistic and physically-based input to the PIC formulations were made available. The MD simulations reported here are a step in the direction and could be extended to include the role of adsorbates, oxides, Maxwell stress induced blowout of sub-surface voids, or sputtering induced defects. A practical validity test for such outgassing predictions might be through comparisons to measured

increases of pressure during high power device operation in test chambers.

An aspect not addressed here, but perhaps important in the context of charged particle incidence upon electrodes in pulsed power systems, could be the time dependent changes in temperature and associated spatial gradients. The latter could add a thermo-diffusive contribution to gas transport, and detailed analysis would require a three-step process of: (i) Initial calculations of the deposited energy from the incident particles, possibly through Monte Carlo calculations with energy-dependent Stopping Power and Mean Free Paths [96], which have been reported elsewhere. (ii) Solutions of heat transport to obtain the evolutionary spatially variable temperature profiles, and (iii) Use of the spatially dependent temperatures thus obtained as inputs in the MD technique to naturally include thermal gradients. The temperature effects could also arise in the context of controlled experiments employing short pulse duration lasers which would give rise to local heating and puffs of emergent gas from the irradiated portions, in addition to features such as possible surface annealing and reconstruction [97]. In this context, it may be mentioned that Molecular Dynamics simulations at high temperatures, for example, a ramp from 300K to 1300K to mimic experimental heating conditions in recent pulsed-power experiments have been reported already [98].

The average planar potential $\bar{V}(z)$ obtained from DFT calculations for a pure copper slab is shown in Figure 12. Apart from this copper-vacuum system, the potential profile for a copper-oxygen-vacuum arrangement is also included in the figure. It should be mentioned that use of such DFT calculations naturally folds in details of the local density of states (LDOS) at the surface. As can be seen from Figure 12, the potential far removed from the surface is a periodic function, with Bloch-like oscillations as expected in a perfect lattice. However, as one gets nearer to the surface, the periodic structure is seen to be perturbed. The result for $\bar{V}(z)$ can thus roughly be broken up into three regions: (i) a zone A that exhibits the periodicity over a region deep into the copper. In Figure 12, this roughly extends from z < ~13.5 Å = z_{min}. (ii) A constant potential over zone C near the interface and away from the copper surface, beyond about 18 Å (= z_{max}), and (iii) an intermediate transition region B roughly between 13.5 Å and 18 Å. In the figure, the work function for the Cu-O system can be seen to be larger than pure copper.

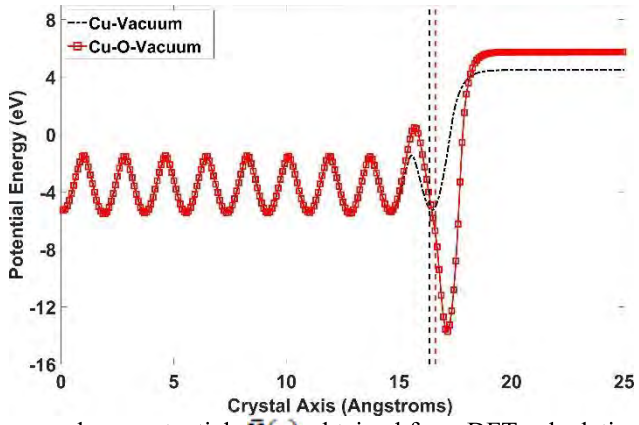

Figure 12. The average planar potentials $\bar{V}(z)$ obtained from DFT calculations for a pure copper slab and a copper-oxygen-vacuum arrangement. The work function for the Cu-O system can be seen to be larger.

Based on the internal potentials, the Schrodinger Wave Equation (SWE) was solved to obtain the electronic wavefunctions for the various cases. The solution involved a numerical

discretization of the SWE, with the entire region being divided into three zones A, B and C. Of these, zone A was at the leftmost end with a zero averaged potential. Zone B was the middle region extending beyond zone A up to the metal-vacuum interface. Finally, zone C constituted the vacuum region. Without any externally applied field, the wavefunctions in Zone C were plane wave states, while appropriate Airy function solutions were assumed in the presence of an external electric field. The Numerov discretization previously discussed was used for zone B, with the usual continuity of $\psi(z)$ and $d\psi(z)/dz$ at its two boundaries. A representative plot of the electronic wavefunction of Cu for (100) copper as a function of distance is shown in Figure 13. This plot was obtained for a normal electron energy E_z value of 7.5 eV with an external electric field of 5 GV/m.

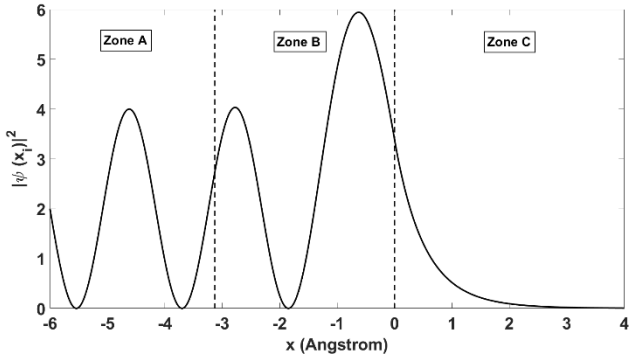

Figure 13. Plot of $|\psi(z)|^2$ as a function of position for the electronic wavefunction of (100) Copper with an external field of 5 GV/m at the normal energy E_z of 7.5 eV.

The current density is related to $T(E_z)$ and the Fermi distribution function $f(E)$ as [99]:

$$J = \iiint [2/(2\pi)^3]\, d^3k\, q\, v_z\ T(E_z)\, f(E)\ . \qquad (6)$$

For a parabolic energy-wavevector relationships [$\hbar^2 k_{||}^2/(2m) = E_{||}$ and $\hbar^2 k_z^2/(2m) = E_z$], the above equation for a thermalized Fermi electron distribution function) simplifies to:

$$J_z = [(qmkT)/(4\pi^2 \hbar^3)] \int_0^\infty dE_z\ T(E_z)\ Ln[1 + exp((E_f - E_z)/(kT))]\ . \qquad (7)$$

A plot of the transmission coefficient $T(E_z)$ is shown in Figure 14 for six different cases. For this calculation, the normal external electric field was set at 5 GV/m. Three plots are for pure copper for the (100), (110), and (111) orientations, and three other curves are with an oxide layer on the copper surface for the same three orientations (denoted as 100o, 110o, and 111o). As evident from the curves, the tunneling coefficient with the oxide layer is smaller than that for pure copper for all three orientations. This is qualitatively expected. With an additional oxide layer, the transmission coefficient reduces as electrons coming from deep inside the material onto the copper surface, face an additional reflective component at the copper-oxide interface.

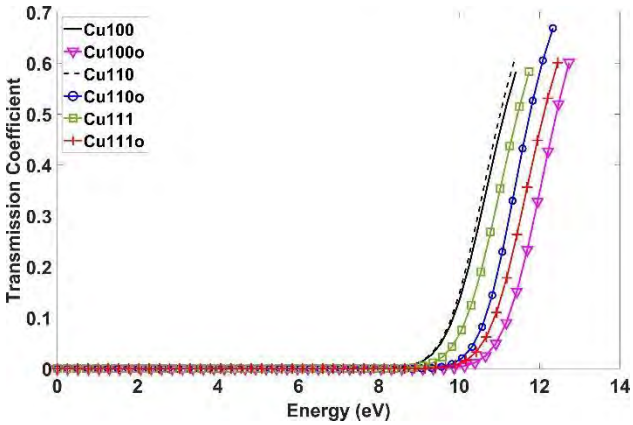

Figure 14. The transmission coefficient as a function of normal electron energy for six different cases, with and without an oxide layer on the copper. The three crystal orientations of (100), (110) and (111) were chosen. The curves for an oxide layer on the copper surface for the same three orientations are denoted as 100o, 110o, and 111o.

The results are shown in Figure 15. As evident from the curves, the current density with the oxide layer is smaller than that for pure copper for all three orientations. This is qualitatively expected since: (i) with an additional oxide layer, the transmission coefficient reduces as already shown as discussed. (ii) Second, the electronegative nature of oxygen, which increases the work function also leads to reduced current emission. Furthermore, from Figure 15 it is evident that the electron emission current should be dependent on the surface orientation.

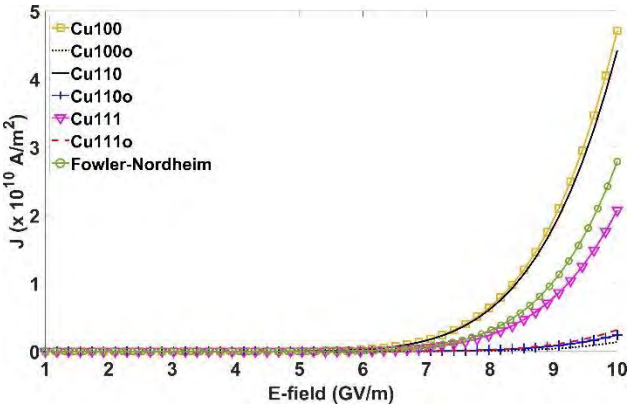

Figure 15. Electron emission current density (J) as a function of external electric field (F) for Cu and Cu-O systems for three different crystal orientations. For comparison, the current density from the usual Fowler-Nordheim model is also shown.

(iii) Currents were calculated for multi-array emitter systems made of tungsten electrodes with cesium or CsI coatings. Time dependent currents were obtained by simulating 19-, 37- and 61-emitter hexagonal arrays as shown in Figures 16(a)-16(c). The distance "d" between the bottom cathode plate and the flat anode was taken to be 2 μm, with the height "h" of each cathode emitter set at 1 μm. Thus, the separation between the emitter tip to anode was 1 μm. The time dependent current calculations carried out for each of the emitter array configurations have been already described in the previous section.

Results of the time-dependent currents obtained for the three hexagonal emitter array structures of Figures 16 are given in Figures 17(a)-17(b) for two different nearest-

neighbor separations. For the currents of Figure 17(a), the separation between nearest-neighbors was set at 0.1 μm, while the curves of Figure 17(b) were obtained for a larger

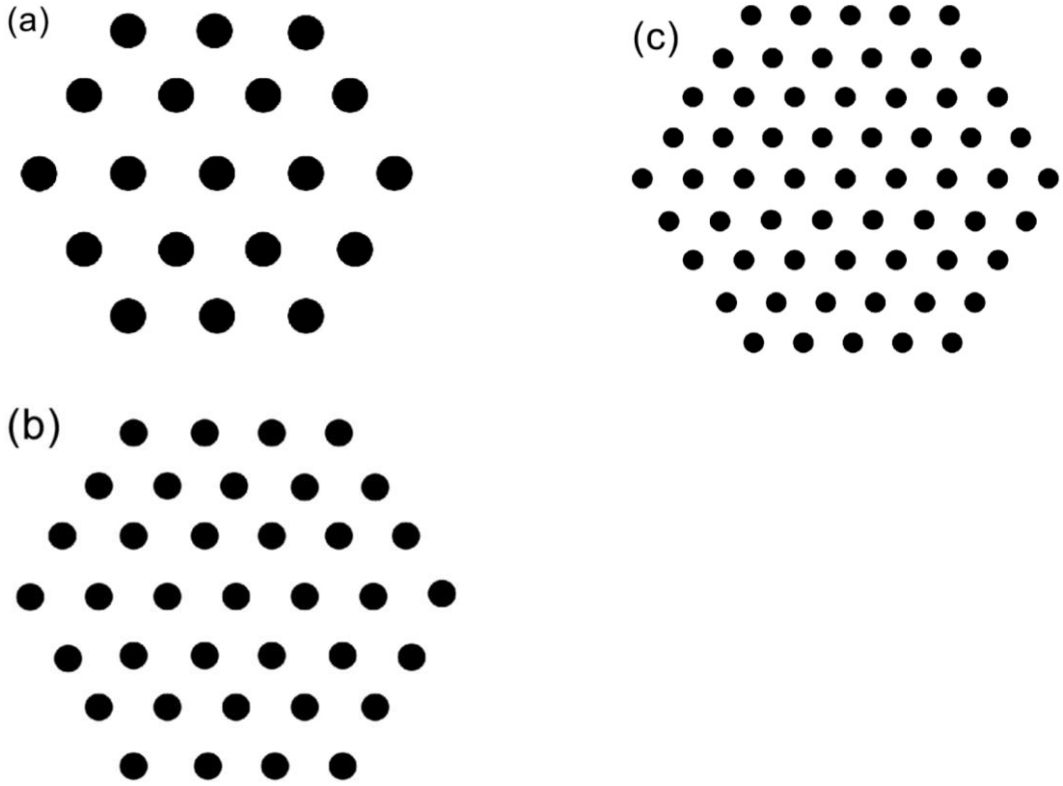

Fig. 16. Arrangement of hexagonal, honeycomb multi-emitter lattice structures. The distance between the cathode base and the flat anode was 2 μm and the emitter heights were taken to be 1 μm. Shown are: (a) a nineteen emitter structure, (b) a 37-emitter array, and (c) a 61-emitter array.

separation of 2.5 μm between adjacent emitters. All cases were for CsI coated tungsten emitter arrays. Two features are evident from the results. First, currents at the smaller 0.1 μm separation are lower as compared to the larger 2.5 μm separation by over a factor of ten. This is the direct result of the proximity effect, as first discussed by Harris et al. [100], which leads to electric field screening. However, the screening is nonuniform with the largest effect felt by the innermost emitter that has the highest number of neighbors. While the largest reduction in effective electric field occurs for the central emitter, the effect becomes progressively milder and decreases going outwards from the array center. The overall current is due to the cumulative contributions from all the individual emitting sources within the array.

In any case, the results of Fig. 17(a) demonstrate that it is not advantageous to place emitters too close together in an array with short nearest-neighbor separations. Though a higher density and larger number of emitters could be realized for a given emitting area, the screening would suppress the currents down to unacceptably low levels. A second

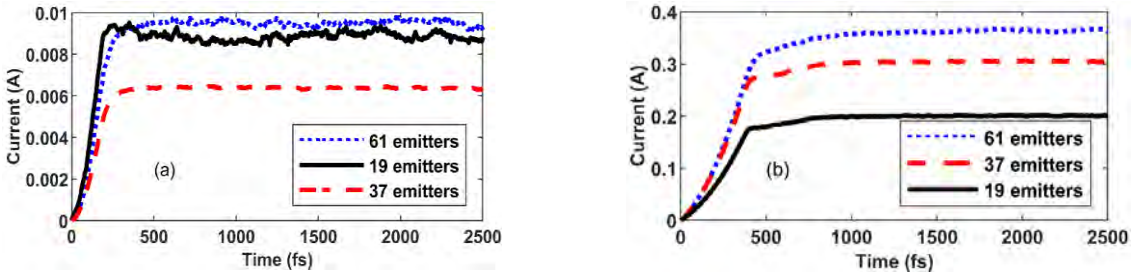

Fig. 17. Time-dependent results for the overall currents for the 19, 37 and 61 CsI coated tungsten emitter arrays with different separations of: (a) 0.1 μm between adjacent emitters, and (b) longer 2.5 μm distance between adjacent emitters.

observation from the plots of Figures 17 is the slightly different direction of current variation with emitter number for the two separations. For the closer packed structure, the lowest current is predicted for the thirty-seven emitter case, with the nineteen emitter scenario yielding higher currents, and the highest value resulting with sixty-one emitters. Thus, in going from nineteen to thirty-seven emitters, the current decreases somewhat from a level of about 9.2 mA to ~6 mA. With nineteen emitters, twelve of the nineteen emitter are at the periphery and so are not subjected to as high a degree of nearest neighbor connectivity. The overall screening effect is then somewhat lower, as compared to the thirty-seven emitter array. However, in going to sixty-one emitters, the overall current is predicted to recover to a slightly higher value of ~9.5 mA. Since progressively less screening is experienced by the outer emitters, and since the increase in emitted current nonlinearly increases with field, the larger number of peripheral cathodes for the sixty-one emitter case collectively contribute to produce a higher overall current than the thirty-seven cathode scenario. In contrast, for the higher 2.5 μm nearest-neighbor separation cases of Figure 17(b), screening and proximity effects are no longer as important. Hence, the overall currents are driven mainly by the number of emitting sources. Consequently, the current output follows a monotonic increasing sequence from nineteen to thirty-seven to sixty-one emitters. These results showing shielding to be negligible for emitter separations larger than 2.5 times the emitter height is similar to the trend first reported by Harris et al. [100] for rectangular arrays. Finally, it may be mentioned that while not shown here, results for the Cs/W arrays were qualitatively similar.

(iv) In the initial calculations of electron emission described and discussed above, the emitting surface was taken to either be flat, or to have a macroscopic curvature based on a paraboloidal or prolate spheroidal or similar shape. However, the electron emission which is controlled to a large extent by the work function (WF), depends on the details of the local atomic environment. The many-body forces surrounding a given emitting atom shape the net local potential and influence the WF. Hence, it is important to tackle this aspect from a microscopic standpoint.

This was done by considering a triangular shape for the emitter as a simple example, as shown in Figure 18 for copper having the 110 orientation. Instead of a true three-dimensional pyramid, a triangular wedge having a periodic extension along one dimension is shown in .

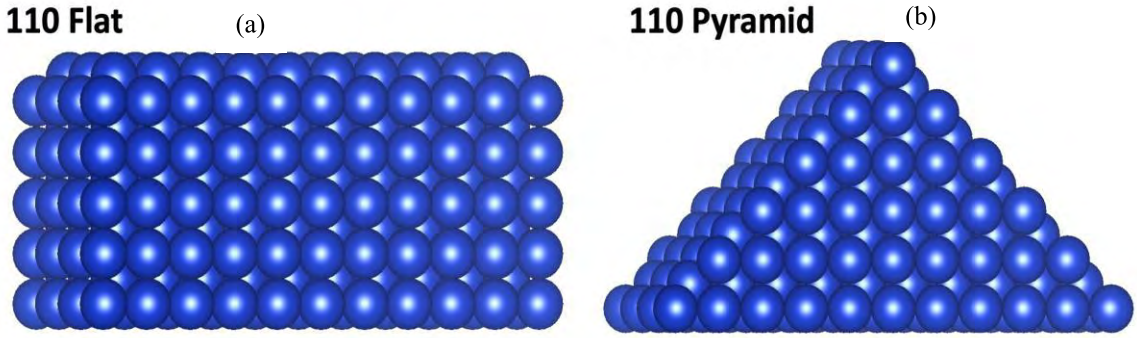

Fig. 18. (a) A three-dimensional ball-and-stick model of a FCC copper lattice, and (b) a two-dimensional pyramidal emitting structure with periodic extension along one axis.

For the wedge-structure, the internal potential and wavefunctions were calculated based on the VASP pseudopotential code. The related projector augmented-wave method and the Perdew-Burke-Ernzerhof parameterized generalized gradient approximation (GGA-PBE) were used to perform all electronic structure calculations. The kinetic energy cutoff was set to 600 eV. As a test, the low-index surfaces (100, 110, and 111) of Cu were used to create three respective pyramidal structures, one for each surface; and their properties compared to a 10-layer flat copper surface shown in Fig. 18(a). The calculated *bulk lattice constant* of Cu (=3.63 Å) was used for all structures. The flat and pyramidal surfaces were made of 10 layers with 70, 65, 67 atoms for the (100), (110), and (111) pyramidal surfaces, respectively. The top three layers of both the flat and pyramidal surfaces were allowed to fully relax and the total Hellmann-Feynman force was seen to be less than $0.01\ eV/Å$ for all structures.

The work functions for all surfaces are given in Table I. The experimental Cu values are provided for comparison along with the work functions for the three pyramidal Cu surfaces. The pyramidal Cu work functions include a slight decrease for the [100] and [110] directions and a particularly large decrease for the [111] direction.

Table I. Calculated work functions (φ) for flat Cu and pyramidal Cu surface orientations using GGA-PBE. Experimental values are given in parenthesis and are from Reference [101].

Surface	Flat Cu (eV)	Pyramidal Cu (eV)
100	4.49 (4.59)	4.48
110	4.39 (4.48)	4.33
111	4.74 (4.92)	4.37

The significant decrease in the work function for the [111] direction can be attributed to the nature of bonding among Cu atoms. Formation energy of surface vacancy can be used as an estimate of the bond strength of surface atoms. In a previous study, the vacancy formation energy was shown to be the highest for the [111] direction, indicating that the (111) surface had the most stable and strongest bond [102]. The (111) pyramid structure that is created by removing the Cu atoms has *dangling* bonds that can reduce the work function of the system. However,

combination with the large packing density of the (111) surface results in an excess number of broken bonds exposing copious amounts of electrons. This reduces the work function significantly with respect to the other two orientations studied here.

In addition to the above statements, the total density of states (TDOS) was used to confirm the effects of removing Cu atoms (for pyramid creation) on the work functions. From the TDOS in Figure 19, a shift in the electronic density is predicted to occur after about -1.6 eV. This shift towards higher energies would make more electrons available for transfer for the pyramidal structure as compared to the flat surface. This effect is separate from any macroscopic field enhancement at the tip due to geometric considerations. Furthermore, as evident from Fig. 19, the TDOS shift is the highest for the [111] direction and lowest for the [100] direction, confirming the trend of the work function change reported in Table 1.

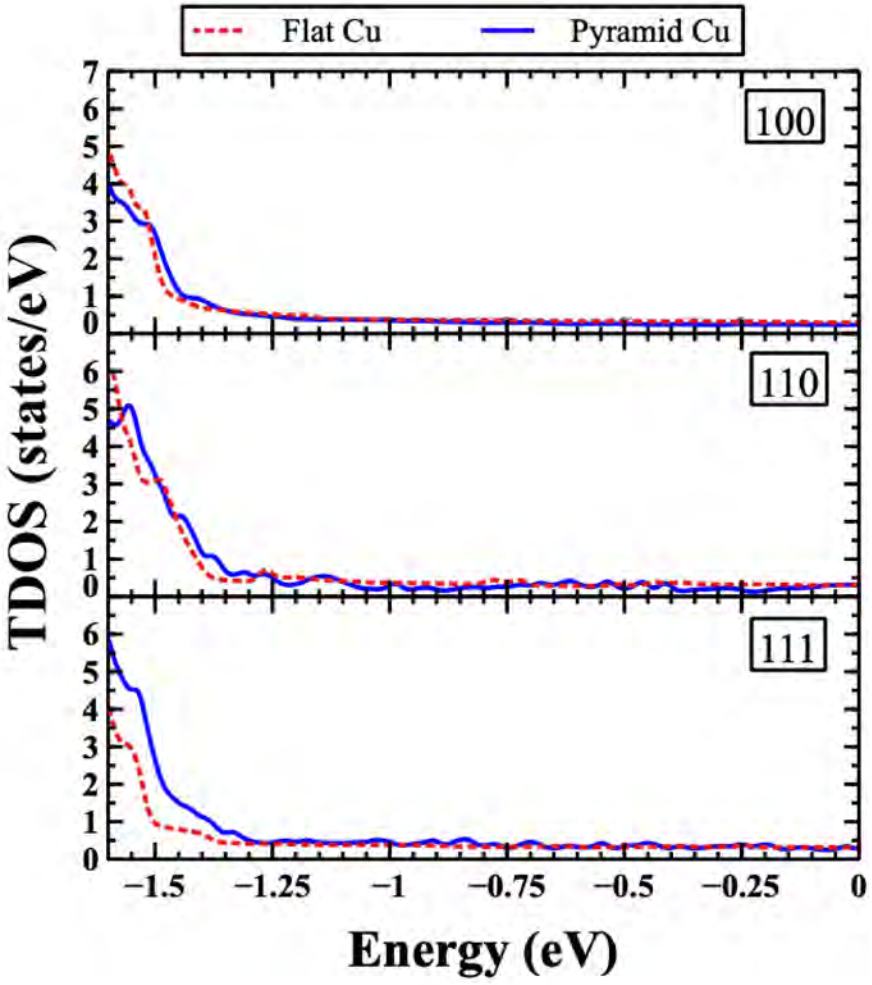

Figure 19. Total density of states for the (100), (110), and (111) flat and pyramid surfaces. The Fermi level is located at E = 0 eV.

Physically, the predicted increase in the electronic transfer possibility and the lowering of the WF (especially in the case of the (111) surface as given in Table I) for the pyramidal structure, arises from the increase in the dangling bonds. Creation of such dangling bonds produces electrons that

are not as strongly bound to the Cu surface. As a result, one anticipates that for all surfaces (regardless of the directional orientation) the electron field emission tunneling current density will be higher for the pyramidal geometries than for the flat surfaces (i.e., $J_F < J_P$, where F and P indicate flat and pyramidal geometries, respectively). While we expect the pyramidal geometries to have a greater current density for all surfaces, it is evident that the [111] direction will see the largest increase due to the largest shift in TDOS and the lowest work function.

The predicted tunneling current density versus surface electric field is shown in Figure 20. The qualitative features discussed in the previous paragraph are borne out in the Fig. 20. Finally, the highest current density is predicted for the pyramidal Cu 100 case.

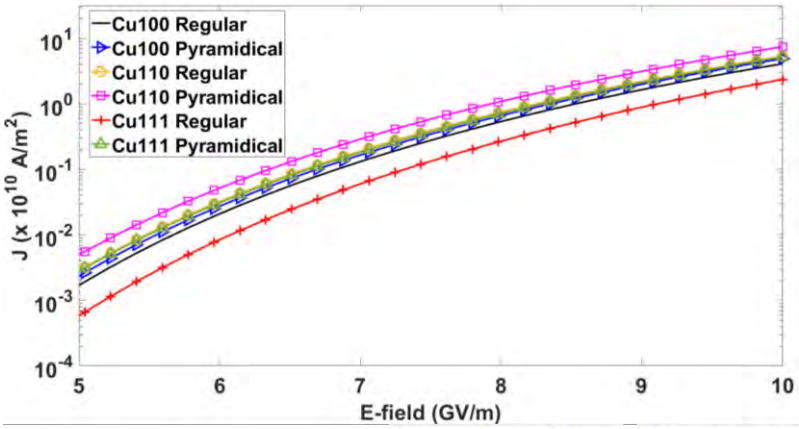

Figure 20. Field emission current density. $J_{110P} < J_{110} < J_{111P} < J_{100P} < J_{100} < J_{111}$.

(v) Since the atomic positions and ordering of C and O atoms in these systems are not known, several configurations of C and O, were studied (Fig. 21). The OC/X system in Fig. 21(a) refers to the case where O is nearest to X (the host substrate) with C being furthest, while the situation is opposite for the CO/X system (Fig. 21(b)). The first-principles total energy calculations identify the OC/X configuration (Fig. 21(a)) as the most stable structure of all the systems. In all of the systems, the adsorbates OC and CO were positioned in a (1 × 1) orientation. For the most stable OC/X structure, the C atoms are closer to the X surface, occupying the short-bridge

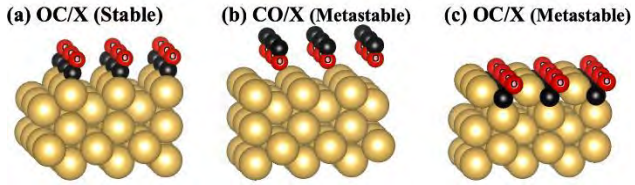

Figure 21. Crystal structures for: (a) stable OC/X, (b) metastable CO/X, and (c) the metastable OC/X. The big gold, small black and small red spheres with small inscribed circle indicate X (X = Cu, Ag, and Au), C, and O, respectively. Calculated energy difference between the OC/X (a) and CO/X (b) were −0.491, −0.121, and −0.231 eV/atom for the Cu, Ag, and Au systems, respectively. The metastable OC/X (c) does not exist for Ag systems and has higher energy with respect to OC/X (a) 0.525 eV/atom for Cu and 0.608 eV/atom for Au systems.

adsorption site, while the O atoms are more distant and sit atop the C atoms. There were two additional metastable structures identified and shown in Figs. 21(b) and 21(c).

Calculated adsorption energies are given in Table II. For Cu, Ag, and Au (110) surfaces, the most stable configuration is the OC/X. The physical reason behind the stability is directly related to the nature of the bonding between C and O atoms. Bader charge analysis [103–106] at the surface confirms a significant charge transfer to the O site mostly from C atoms. Calculated electronic charge transfer to O site was 1.72 (OC/Cu), 1.86 (OC/Ag), and 1.84 (OC/Au), respectively, for the Cu, Ag and Au systems. As a result of such a transfer, large dipole moments were created, and the resulting values of the dipole moments perpendicular to the surface ($p_\perp$) are included in Table II. Therefore, C and O atoms are almost exclusively bonded to each other. The nature of the bonding between C-O and X surfaces should be a result of the interactions of the CO dipole with the X surface (dipole-induced dipole interactions). Furthermore, one can also explain the physical reason of the higher adsorption energy of the CO/X with respect to the OC/X based on the small dipole moment of the CO/X systems.

Table II. Calculated zero-temperature adsorption energies ΔH (eV/atom), work functions ϕ (eV), perpendicular dipole moments $p_\perp$ (eÅ), and Fermi level energy E_F (eV) for the transition metal substrates X (X = Cu, Ag, and Au), CO/X, and OC/X. Experimental work functions are provided for comparison.

110 Surface	ΔH (eV/atom)	Φ_{cal} (eV)	$p_\perp$ (eÅ)	E_F (eV)
Cu	n/a	4.40 (4.48[a])	n/a	8.91
OC/Cu	-2.795	6.07	.01135	10.66
CO/Cu	-2.304	4.95	0.0391	10.12
Ag	n/a	4.16 (4.14[b])	n/a	7.26
OC/Ag	-2.546	5.28	0.1025	10.18
CO/Ag	-2.425	4.54	0.0260	10.31
Au	n/a	4.98 (5.12[c])	n/a	7.25
OC/Au	-2.659	5.88	0.0851	11.89
CO/Au	-2.428	4.97	-0.0036	9.81

[a]Reference [107]. [b]Reference [108]. [c]Reference [109].

One of the required parameters of the Monte Carlo secondary electron emission simulation is the work function, which is dependent on the charge density of the surface.

The calculated work function and the Fermi level energy for all of the systems were compared with available experimental data, and are provided in Table I. From Table I, one can see a direct correlation between the work function and the dipole moment. The role of the dipole moment in influencing the work function is well known [110], and was invoked to explain the role of coatings on field emitters [74]. The larger the dipole moment, the greater the work function change. Interestingly, for the CO/Au system the work function is slightly smaller than the clean Au surface. This is in agreement with the reversal of the dipole moment direction with respect to some of the other systems. Furthermore, the calculated work function values for all three clean metals in Table I are in good agreement with published data. The work functions, Fermi energies, and dielectric functions were used as input parameters to calculate the inelastic mean free paths (IMFP) and secondary electron emissions (SEY). For the rest of this work, we will only study and discuss the most stable OC/X structure given in Fig. 21(a).

Results of the inelastic mean free path (IMFP) for the Cu, Au, and Ag (110) surfaces are shown in Fig. 22. As one can see from the figures, the calculated IMFP's show very good agreement with experimental measurements [111–113]. The addition of the OC layers to all of the clean surfaces causes a decrease in the IMFP across the entire energy spectrum (Fig. 22). The physical reason of the IMFP decrease is directly related to change of the density of states (bonding between C, O and X) that will be discussed shortly.

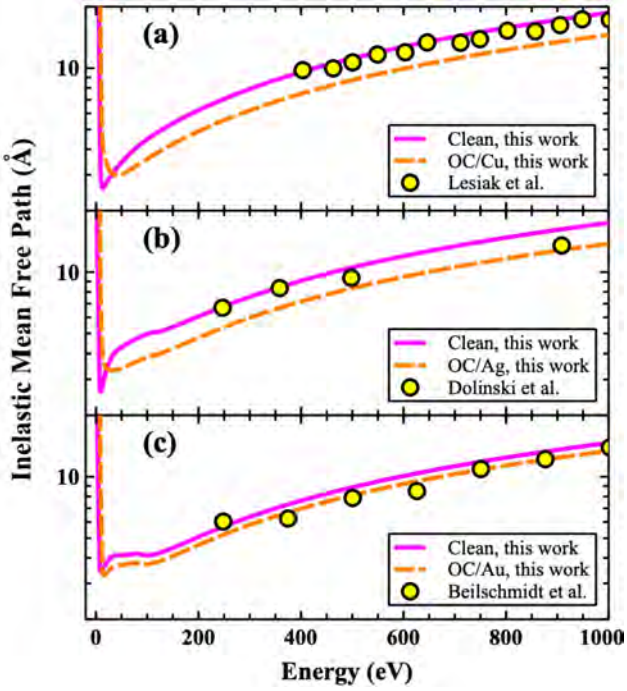

Figure 22. Inelastic mean free paths for: (a) Cu, (b) Ag, and (c) Au systems. Experimental results are also provided for comparison including Lesiak et al. [111], Dolinski et al. [112], and Beilschmidt et al. [113] for Cu, Ag, and Au, respectively.

The SEY calculations of the clean and OC/X structures are shown in Fig. 23 and are compared with available experimental results [71-73, 114]. An overall agreement

between the simulated and experimental measurements can be seen in all of the plots of Fig. 23. Also, the presence of the OC adsorbate is predicted to significantly increase the SEY for all of the systems. The origin of the slight differences is likely related to the use of polycrystalline samples [71-73] instead of the high symmetric surfaces used in this study. Additionally, minor deviations could also stem from the presence of other impurities in the actual experimental samples and their possible two-dimensional distributions along the surface. Variations in lateral distribution under experimental conditions such as partial or nonuniform coverage of the surface can also influence the SEY outcomes. Furthermore, the "as received" sample could have had other impurities in them such as N, H_2O, NO, CO_2 etc. Moreover, the present calculations assumed a smooth surface with no roughness and an ideal uniform-distribution of OC at the top surface, which could be different from the actual samples tested. For example, roughened surfaces could have mini-terraces or numerous small tilts. For a surface having a small angular tilt α, the threshold condition in equation (1a) would change to: $E\cos^2(\theta-\alpha) > U_0$. As a collective result, smaller energies would be allowed to pass over the threshold, and the overall SEY value would increase due to surface tilts or corrugation, as in the measured data. Despite all of the possible variability, however, the present calculations do demonstrate reasonable agreement with data, and also show that the addition of O and C adsorbates at the surface could be a source of SEY enhancements. The results also suggest that cleaning the sample surfaces to get rid of the O and C adsorbates might be beneficial for SEY lowering. Furthermore in Fig. 23, the strongest deviation between clean material and the SEY predictions with and O and C absorbates included, is for silver and gold.

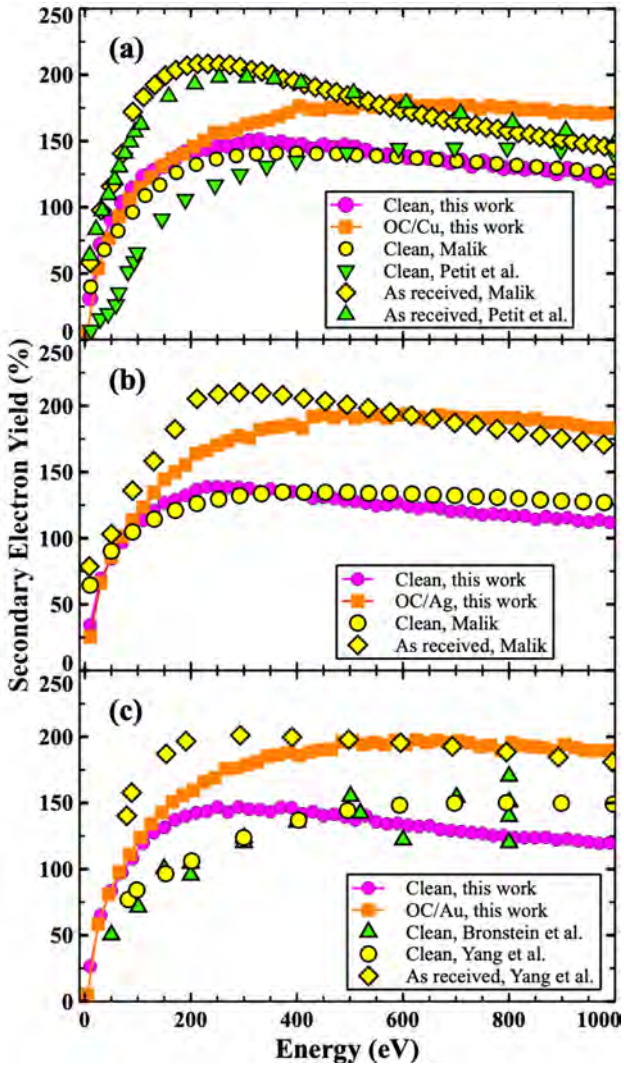

Figure 23. Secondary electron yield for three system: (a) Cu, (b)Ag, and (c) Au systems. Experimental measurements are also provided for comparison including the results from Petit et al. [71], Yang et al. [72], Malik [73], and Bronstein et al. [114].

Accomplishments

(i) Research Objectives:

The main research objectives and goals of this project focus on simulations and basic research for understanding fundamental details of breakdown under RF conditions, and processes at the cathode such as electron emission, outgassing, role and effect of surface-conditioning, and breakdown under RF conditions for vacuum electronics and high power applications. Details relating to space-charge, proximity- and density-dependent dynamic screening, out-gassing and plasma formation were probed based on many-body charge transport coupled with the Fast Multipole Method, as they all directly affect the

efficiency and reliability of high power microwave (HPM) systems. Comprehensive electron emission included evaluations of material properties (e.g., workfunction), and internal potentials that were folded into the Schrodinger Wave Equation for transmission probability analysis. In addition, surface changes (e.g., oxide over-layer, adsorbates) that alter material work function, thus adversely impacting electron emission, are also studied based on Density Functional Theory. Additionally, the effort this year included simulations to study carbon fibers, which were shown to significantly reduce outgassing. Finally, geometric variations in emitter structures from an atomistic standpoint, not just macroscopic field enhancements, were considered through numerical analysis.

For all of the above tasks, appropriate comparisons with experimental data or published results in the literature were carried out to the extent possible for verification and validity.

(ii) Details of accomplishments:

Major activities:
Modeling and simulation based on: (i) the Monte Carlo method for transport in air in millimeter gaps, (ii) Coupled Monte Carlo and Density Function Theory for evaluation of secondary electron emission in various materials, (iii) Molecular Dynamics for hydrogen outgassing from copper and carbon fibers, (iv) Comprehensive calculations of time-dependent electron emission currents from emitter arrays based on analysis of electric fields with inclusion of mutual screening, field emission and space-charge transport incorporating the Fast Multiple Method for self-consistent electric field calculations.

Specific objectives:
Obtain prediction and carefully compare results with available data and measurements for:

(i) Probe breakdown voltage as a function of .gap length with and without the presence of photons to quantify the possible role of photoemission on the gas breakdown. Unlike previous studies of RF breakdown, the role of photon-emission processes is explicitly included and shown to be important for large area electrode configurations. Numerical analysis based on Monte Carlo calculations is used to predict the breakdown thresholds, by quantifying the fields at which the electron population remains nearly invariant. The simulations embed a statistical photon transport model, based on random selections of emission angles and times from excited atoms, as well as photoemission from the electrodes.

(ii) Values of electron work function for different materials such as: (a) pure copper with crystal in the (100), (110) and (111) orientations, (b) copper coated with Cs, (c) Tungsten as an emitter, (d) copper with an oxide film, (e) nickel, and (f) gold and silver with and without surface carbon and oxygen absorbates.

These values were needed for predictions of electron emission and related currents in emitter-arrays. The calculations were based on the use of Density Functional Theory (DFT).

(iii) Obtain outgassing and to quantify temperature-dependent diffusion coefficient of hydrogen gas in various materials based on the Molecular Dynamics technique. Copper, copper coated with cesium and carbon fibers were evaluated, as well as the possible coating of tungsten for reductions in outgassing. Values of the hydrogen diffusion coefficients were predicted in a large operating range from 300K to 1200 K.

(iv) Evaluation of currents in emitter arrays to probe the role of screening, and to quantify the predicted behavior as a function of the number of emitters and the nearest neighbor separation. Both uniform arrays as well as different arrangements of bimodal emitters were probed.

Significant results:
A summary of the results obtained is given below.

(i) The behavior of the breakdown electric field versus gap lengths (in the 1-5 mm range) and different frequencies in the 1 - 80 MHz span were studied numerically at atmospheric pressure. Simulation results compare well with experimental data from our group, but only with inclusion of photon processes. Though both photoemission and photoionization are included in the breakdown physics, the former is identified as the dominant process. The frequency behavior of breakdown fields is also assessed with inclusion of photons, and the results reveal a U-shaped trend with increasing values for smaller gaps.

(ii) Work function values were obtained from Density Functional Theory (DFT). In all of the cases studied, the predictions for pure material were in close agreement with reported values. This was the case for copper [all three orientations of (100), (110) and (111)], nickel, tungsten, and cesium-coated copper. In addition, values were also obtained for Cs and CsI coated tungsten electrodes.

(iii) The predicted values obtained matched experimental data on hydrogen diffusion coefficients in copper over the 300K – 1200 K range over six orders of magnitude.

In addition, evaluation of hydrogen outgassing from carbon fibers revealed about a two-orders of magnitude reduction as compared to the out-diffusion values in copper. This is significant and points to the advantage in using carbon fibers as electrode material for mitigating outgassing.

Finally, the emission of hydrogen puffs were predicted from copper on sub-microsecond time scales. In cases of elevated temperature operation (e.g., 1000 K), hydrogen outgassing was predicted at times as low as 40 ns. These short emission times are roughly in keeping with experimental reports of outgassing related plasma formation from Sandia's Z-machines.

(iv) Analysis of field emission requires inclusion of the internal potentials which shape the electronic wavefunctions and tunneling probabilities; details of the work function which is dependent on material quality and defects; and the role of

density of states (DOS) which influence the electronic supply. In our work, these factors are collectively included on the basis of Density Functional Theory, to obtain predictions of field-dependent electron tunneling current densities. Results were obtained in copper for three different orientations. The DOS was predicted to be broadened by an externally applied electric field. The (100) copper was shown to yield the largest current density, and (111) orientation the lowest. The presence of an oxide surface monolayer (ML) was shown to increase the work function, leading to emission current reductions. The technique is general and was later applied to other materials (e.g., tungsten, Cs-coated copper emitters, and carbon fibers) that have shown promise as cathode emitters.

Evaluations of electron current output from tungsten emitter arrays with Cs and CsI coatings are carried out. The approach was based on first-principles calculations of the material physics including evaluation of the internal potentials, electronic wavefunctions, tunneling probabilities, and work function to predict field emission currents. This was coupled to time-dependent kinetic simulations for the assessment of emitter array currents with an inclusion of many-body Coulomb contributions from the electron swarm, geometric field enhancements with shielding based on a line charge model and dynamic screening from the swarm. Our numerical evaluations for arrays with a hexagonal lattice showed the expected role of field screening with reductions in emitter separation. For scaling with emitter number, the results indicate nearest neighbor separations of more than 2.5 times the emitter height, in keeping with previous reports. Also, different patterns were examined within a hexagonal lattice structure. For a bimodal distribution, output current optimization was shown for alternating arrangements with three or more successive emitters of the same length along primitive axes predicted to have an advantage.

All set goals were met.

(iii) Result dissemination:

The results were widely disseminated in scientific and engineering circles through two important ways:

(a) Appropriate journal publications that could reach a global audience. A total of 12 journal articles were published as the direct result of this grant funding over the course of three years. Details are given in the early part of this report.

(b) Conference presentations that also helped disseminate ideas and results to the scientific community. The conferences at which our ideas were presented and discussed included: (i) Pulsed Power and Plasma Science (PPPS) Conference in 2019 at Orlando, (ii) International Vacuum Nanoelectronics (IVNC) and International Vacuum Electron Sources (IVESC) Conferences in 2019, (iii) Pulsed Power Conference in 2021, (iv) International Power Modulators and High Voltage Conference (IPMHVC) in 2022.

Impacts

Development of the principal discipline(s) of the project

(i) The molecular dynamic simulations of gas diffusion and outflow presented perhaps for the first time, calculations on outgassing from an atomistic standpoint. Most previous reports used either experimental data, or relied on continuum theory for which the transport coefficients (such as the diffusion constant) were unknown. Furthermore, analyses based on this technique, temperature dependent values in different materials – copper, cesium, and carbon fibers were all studied. Finally, role of internal vacancies in arresting or reducing the gas diffusion was also probed and temperature-dependent quantitative prediction made.

(ii) Second, the field emission of electrons obtained on this study explicitly included details of the workfunction (WF) at the surface, electron transmission probability based on the wavefunctions dictated by the local potentials. The WF was calculated from Density Functional Theory for copper, carbon fibers and cesium, and could easily be extended to any material of interest. For self-consistency, results of the DFT calculations were folded into evaluations of electron transmission from the material into vacuum by solving for the wavefunctions based on the local potentials at the surface from the DFT. The potentials were incorporated in a time-independent Schrodinger Equation for the wavefunctions, which were then used to yield the currents. Thus, material details and internal structure were comprehensively incorporated.

(iii) Third, for current calculations from emitter arrays, the Linear Charge Model (LCM), already published in the literature, was used for the local field calculations. However, the fields were then used with the above DFT-based emission current calculations for self-consistency. Furthermore, dynamic screening of the emitted electro swarm from the cathode arrays was taken int account for the first time. This method can be usefully applied to other current calculations involving high-density swarm kinetics.

(iv) The role of thermal conductivity of carbon fibers was also evaluated. Numerical simulations yielded values for bulk material close to the measured values of ~15 W/m/K However, due to finite-size effects, the thermal conductivity was seen to reduce dramatically with decreases in emitter length. *The results suggest that in order to ensure that thermal conductivity does not fall to low values, emitter samples larger than 2 μm should be used.*

(v) Finally, the physics behind reduction in Secondary Electron Yield (SEY) upon surface treatment and cleaning has been explained on a theoretical footing. It has been shown that the presence of carbon (C) and oxygen (O) is responsible for increased SEY. Three factors have been shown to play a role: (a) changes in work function, (b) reductions in the inelastic mean free path, and (c) changes in the density of states. By utilizing the approach proposed in our work (M. Brown, L. Diaz, A. Aslan, M. Sanati, S. Portillo, E. Schamiloglu, and R. P. Joshi, "Carbon-Oxygen Surface Formation Enhances Secondary Electron Yield in Cu, Ag and Au: A coupled first-principles, Monte Carlo Analysis," submitted for publication, 2022), it would be possible to pin-point the material most likely responsible for SEY increases and work to eliminate such elements or compounds through appropriate cleaning, heat treatments or processing.

In conclusion, numerous tasks performed were all aimed at improving the modeling capability of high power microwave devices. A fundamental physics-based understanding of emission processes lay at the heart of the analysis. *The tools developed would allow for experimental comparisons (for example with carbon fiber cathodes), and to tailor and optimize system performance of HPM systems.*

Other disciplines:
One of the team members of this project is Dr. M. Sanati in the Physics Department at Texas Tech University (TTU). One of the graduate students in Physics in Dr. Sanati's class (Leopold Diaz of Hispanic ethnicity) got interested in the project and decided to apply the Density Functional Theory that was being taught in his Physics class to aspects of this project. He used the DFT techniques to compute the work functions of copper and carbon fibers.

Other students in Dr. Sanati's graduate class in the Physics Department are also now aware of and becoming interested in this research.

Describe the impact in this reporting period on the development of human resources
As the direct result of the project, a student (Madeline Brown) from Physics at Texas Tech University (TTU) chose to come over and join the Graduate Program in Electrical Engineering at TTU. Madeline is a Woman in Engineering and has joined the PhD program since Fall 2021. Though not formally working on the project to start with, as she was currently supported by the College, and she started to learn Monte Carlo simulations. In a relatively short time (Summer and Fall semesters), Madeline has generated some very good results of Secondary Electron Emission for nickel, and the data was being put together for a journal. This contributed and published -- M. Brown, M. Sanati, and R. P. Joshi, "Combined First Principles-Monte Carlo Analyses to Evaluate the Effect of Surface Hydrogen on the Secondary Electron Yield of Nickel," Journ. Appl. Physics **131**, 103301 (2022). In addition, Madeline has worked on and is a first author on two manuscripts that have been submitted and are under review. These two manuscripts are: (i) M. Brown, W. Milestone, and R. P. Joshi, "Monte Carlo Analysis of Electron Trapping in Nested Groove Structures for Mitigation of Secondary Electron Emission for Potential Multipactor Control in Waveguides," submitted for publication, and (ii) M. Brown, L. Diaz, A. Aslan, M. Sanati, S. Portillo, E. Schamiloglu, and R. P. Joshi, "Carbon-Oxygen Surface Formation Enhances Secondary Electron Yield in Cu, Ag and Au: A coupled first-principles, Monte Carlo Analysis," submitted for publication.

Besides, Madeline also interacts with other students in the Pulsed Power Laboratories at TTU, who are experimentalists and practitioners, to learn and get familiar with various aspects of Pulsed Power and related engineering physics.

Describe the impact on teaching and educational experiences
The project had some minor influence on the content of two graduate-level courses at Texas Tech university. (i) In the Engineering Analysis (ECE 5371), concepts relating to Molecular Dynamics were introduced, and a student chose a Term Paper on MD applications. (ii) In Solid State Devices (ECE 5314), student learnt about field emission and from emitter arrays, the issue of charge screening, and one student chose a Term Paper on Nano-emitter Field Arrays for the class.

Some results obtained in the project on both MD simulations and field emitters were used in lectures as part of teaching, and emphasized real applications to current research problems. Both

courses were online in 2020 and 2021, aimed at higher enrollments and to offer flexibility and convenience to students.

Describe the impact in this reporting period on physical, institutional, and information resources that form infrastructure.
None.

Impact on society beyond science and technology:
None.

Changes

Changes in approach
There were minor changes in the detailed focus of the project. Based on the possible applications and the need to better understand the inherent physics which impact and contribute to the overall efficiency and reliability of high power devices, more emphasis was placed on various processes such as electron emission, out-gassing, space-charge and proximity effects, and their contributions to the overall currents and electron emission.

In addition, the role of out-gassing as also probed, as was the effect of absorbates and surface contamination on secondary electron yields. In a way, more in-depth physics and fundamental processes were included. These topics have a direct relevance to and bearing on High Power Microwave and Pulsed Power system development.

Problems or delays
Due to COVID 19, there were slight delays as the university was closed for some time during part of 2020 and 2021. Adjustments to the schedule, returning back to work, students having to set up computers at home, learning to communicate via Zoom etc., took time and adjustment. For these reasons this 3-year project was slightly delayed. So instead of the January 2019-December 2021, the project spanned January 2019-May 2022.

Expenditure Impacts
No changes.

Significant changes in the use or care of human subjects, vertebrate animals and/or biohazards
No changes, not applicable.

Changes to the primary place of performance from that originally proposed
No changes.

Technical Updates

None.

References

1. G. V. Naidis, Plasma Sources Sci. Technol. **15**, 253 (2006).
2. J. Dutton, S. C. Haydon, and F. L. Jones, Proc. R. Soc. A **218**, 206 (1953).
3. M. B. Zheleznyak, A. Kh. Mnatsakanyan, and S. V. Sizykh, High Temp. **20**, 357 (1982).
4. N. Yu. Babaeva and G. V. Naidis, J. Phys. D: Appl. Phys. **29**, 2423 (1996).
5. A. Bourdon, V. P. Pasko, N. Y. Liu, S. Celestin, P. Segur, and E. Marode, Plasma Sources Sci. Technol. **16**, 656 (2007).
6. S. Nijdam, F. M. J. H. van de Wetering, R. Blanc, E. M. Veldhuizen, and U. Ebert, J. Phys. D: Appl. Phys. **43**,145204 (2010).
7. A. Fierro, G. Laity, and A. Neuber, J. Phys. D: Appl. Phys. **45**, 495202 (2012).
8. Z. Xiong and M. J Kushner, Plasma Sources Sci. Technol. **23**, 065041 (2014).
9. G. Wormeester, S. Pancheshnyi, A. Luque, S. Nijdam, and U. Ebert, J. Phys. D: Appl. Phys. **43**, 505201 (2010).
10. A. Luque and U. Ebert, Phys. Rev. E **84**, 046411 (2011).
11. A. Luque and U. Ebert, J. Comput. Phys. **231**, 904 (2012).
12. A. Fierro, J. Stephens, S. Beeson, J. Dickens, and A. Neuber, Physics of Plasmas **23**, 013506 (2016).
13. R. B. Hutchison, Journal of Quantitative Spectroscopy and Radiative Transfer **11**, 81 (1971).
14. W. K. Bischel, B. E. Perry, and D. R. Crosley, Chemical Physics Letters **82**, 85 (1981).
15. G. Bengtsson, J. Larsson, S. Svanberg, and D. D. Wang, Physical Review A **45**, 2712 (1992).
16. N. Zheng and T. Wang, The Astrophysical Journal Supplement Series **143**, 231 (2002).
17. J. Musielok, W. L. Wiese, and G. Veres, Physical Review A **51**, 3588 (1995).
18. A. Kramida, Yu. Ralchenko, J. Reader, and NIST ASD Team, *NIST Atomic Spectra Database* (version 5.6.1), National Institute of Standards and Technology (Gaithersburg, MD, 2018). DOI: https://doi.org/10.18434/T4W30F
19. E. D. Lozansky and O. B. Firsov, Theory of Sparks (Atomizdat, Moscow, 1975).
20. B. Camino, T.C.Q. Noakes, M. Surman, E.A. Seddon, and N. M. Harrison, Computational Materials Science **122**, 331 (2016).
21. J. P. Verboncoeur, Plasma Phys. Control. Fusion **47**, A231 (2005).
22. J. P. Boeuf and E. Marode, J. Phys. D **15**, 2169 (1982).
23. A. Phelps and L. Pitchford, *JILA Information Centre Report 26.* Colorado, USA, 1985.
24. Y. Itikawa, M. Hayashi, A. Ichimura, K. Onda, K. Sakimoto, K. Takayanag, M. Nakamura, H. Nishimura, T. Takayanagi, Journal of Physical and Chemical Reference Data **15**, 985 (1986).
25. Y. Itikawa, Journal of Physical and Chemical Reference Data **38**, 1 (2009).

26. P. Rumbach and D. B. Go, J. Appl. Phys. **112**, 103302 (2012).
27. D. B. Go and A. Venkattraman, J. Phys. D **47**, 503001 (2014).
28. J. M. Torres and R. S. Dhariwal, Nanotechnology **10** 102 (1999).
29. N Liu and V P Pasko, J. Phys. D: Appl. Phys. **39**, 327 (2006).
30. For example, I. A. Kossyi, A. Yu. Kostinsky, A. A. Matveyev, and V. P. Silakov, Plasma Sources Sci. Technol. **1**, 207 (1992).
31. L. Gallmann, I. Jordan, H. J. Worner, L. Castiglioni, M. Hengsberger, J. Osterwalder, C. A. Arrell, M. Chergui, E. Liberatore, U. Rothlisberger, and U. Keller, Structural Dynamics **4**, 061502 (2017).
32. W. Theil, Chemical Physics **57**, 227 (1981).
33. J. Stephens, M. Abide, A. Fierro, and A. Neuber, Plasma Sources Sci. Technol. **27**, 075007 (2018).
34. For example, K. Wood, J. S. Mathis, and B. Ercolano, Mon. Not. R. Astron. Soc. **348**, 1337 (2004).
35. M. A. Furman and M. T. F. Pivi, Phys. Rev. Accel. Beams **5**, 124404 (2002).
36. H. K. A. Nguyen, J. Mankowski, J. Dickens, A. Neuber, and R. P. Joshi, IEEE Trans. Plasma Sci. **47**, 1364 (2019).
37. I. A. Aponte, B. Esser, Z. C. Shaw, J. C. Dickens, J. J. Mankowski, and A. A. Neuber, Physics of Plasma **26**, 123512 (2019).

38. VASP 2003 at *http://www.vasp.at*.
39. P. E. Blöchl, O. Jepsen, and O. K. Andersen, Phys. Rev. B **49**, 16223 (1994).
40. G. Kresse and J. Hafner, Phys. Rev. B 47, 558(R) (1993).
41. G. Kresse and J. Furthmüller, Phys. Rev. B **54**, 11169 (1996).
42. D. Vanderbilt, Phys. Rev. B **41**, 7892(R) (1990).
43. J. P. Perdew, K. Burke, and M. Ernzerhof, Phys. Rev. Lett. **77**, 3865 (1996).
44. H. J. Monkhorst and J. D. Pack, Phys. Rev. B **13**, 5188 (1976).
45. J. R. Harris, K. L. Jensen, D. A. Shiffler, and J. J. Petillo, Applied Phys. Lett. **106**, 201603 (2015).
46. D. Biswas, G. Singh, and R. Kumar, J. Appl. Phys. **120**, 124307 (2016).
47. E. M. Vinogradova, E. N. Egorov, and D. S. Televnyy, Vacuum **127**, 45 (2016).
48. E. Mesa, E. Dubado-Fuentes, and J. J. Saenz, J. Appl. Phys. **79**, 39 (1996).
49. D. Guo, S. N. Sami, and R. P. Joshi , AIP Advances **9**, 105302 (2019).
50. J. R. Harris, K. L. Jensen, W. Tang, and D. A. Shiffler, Journ. Of Vacuum Science and Technol. B **34**, 041215, 2016.
51. B. V. Numerov, *Astronomische Nachrichten* **230**, 359–364 (1927).
52. C. K. Birdsall and A. B. Langdon, in Plasma Physics via Computer Simulation (MacGraw Hill, N. York, 1985).
53. T. Takizuka and H. Abe, Journ. Computational Phys. **25**, 205 (1977).
54. Y. Weng and M. J. Kushner, Phys. Rev. A **42**, 6192 (1992).
55. P. Lugli and D. K. Ferry, IEEE Trans. Electron Devices **32**, 2431 (1985).
56. R. P. Joshi and D. K. Ferry, Phys. Rev. B **43**, 9734 (1991).
57. P. Menziani, F. Rossi, and C. Jacoboni, Solid-State Electron. **32**, 1807 (1989).
58. D. Vasileska, S. M. Goodnick and G. Klimeck, in Computational Electronics: Semiclassical and Quantum Transport Modeling (Taylor and Francis, Boca Raton, 2010).
59. R. W. Hockney and J. W. Eastwood, *Computer Simulation Using Particles* (New York, McGraw-Hill, 1981).
60. W. J. Gross, D. Vasileska and D. K. Ferry, IEEE Electron Device Lett. **20**, 463 (1999).

61. C. J. Wordelman and U. Ravaioli, IEEE Trans. Electr. Dev. **47**, 410 (2000).
62. V. Rokhlin, J. Computational Physics **60**, 187 (1985).
63. R. Beatson and L. Greengard, "A short course on fast multipole methods," in Wavelets, Multi-level Methods and Elliptic PDEs (Leicester, 1996), ser. *Numer. Math. Sci. Comput*. (Oxford Univ. Press, New York, 1997), pp. 1–37.
64. http://www.scafacos.de/files/pub/libfcs_manual.pdf
65. A. Arnold, F. Fahrenberger, C. Holm, O. Lenz, M. Bolten, H. Dachsel, R. Halver, I. Kabadshow, F. Gähler, F. Heber, J. Iseringhausen, M. Hofmann, M. Pippig, D. Potts, and G. Sutmann, Phys. Rev. E **88**, 063308 (2013).
66. S. Plimpton, J. Comput. Phys. **117**, 1 (1995).
67. Z. Bashir, Carbon **29**, 1081 (1991).
68. F. Khabaz, I. Rafikul, and R. Khare, "Thermal conductivity of polymer nanocomposites: applications of molecular dynamics simulations," in *Thermal Behaviour and Applications of Carbon-Based Nanomaterials: Theory, Methods and Applications,* Ed.: D. V. Papavassilios, H. M. Duong, and F. Gong (Elsevier, N. York, 2020), p. 305-324.
69. P. V. Gulgunje, B. A. Newcomb, K. Gupta, H. G. Chae, T. K. Tsotsis, and S. Kumar, Carbon **95**, 710 (2015).
70. R. E. Davies and J. R. Dennison, Journal of Spacecraft and Rockets **34**, 571 (1997).
71. V. Petit, M. Taborelli, H. Neupert, P. Chiggiato, and M. Belhaj, Phys. Rev. Accel. Beams **22**, 083101 (2019).
72. J. Yang, W. Cui, Y. Li, G. Xie, N. Zhang, R. Wang, T. Hu, and H. Zhang, Appl. Surf. Sci. **382**, 88 (2016).
73. T. A. Malik, Secondary Electron Yield Measurements on Materials of Interest to Vacuum Electron Communication Devices, MS Thesis, University of New Mexico (2020).
74. D. Guo, S. N. Sami, L. Diaz, M. Sanati, and R. P. Joshi, Journal of Vacuum Science and Technology B **39**, 054201 (2021).
75. S. N. Sami, L. Diaz, M. Sanati, and R. P. Joshi, Journal of Applied Physics **128**, 223302 (2020).
76. H. K. A. Nguyen, M. Sanati, and R. P. Joshi, Journal of Applied Physics **126**, 123301 (2019).
77. P. S. Bagus, V. Staemmler, and C. W¨oll, Phys. Rev. Lett. **89**, 096104 (2002).
78. L. Zheng, R. P. Joshi, and C. Fazi, Journal of Applied Physics **85**, 7935 (1999).
79. M. Bhatnagar, P. McLarty, and B. J. Baliga, IEEE Electron Device Letters **13**, 501 (1992).
80. J. H. Werner and H. H. G¨uttler, Journal of Applied Physics **73**, 1315 (1993).
81. D. R. Penn, Phys. Rev. B **35**, 482 (1987).
82. M. Brown, M. Sanati, and R. P. Joshi, J. Appl. Phys. **131**, 103301 (2022).
83. X. Qiu, L. Diaz, M. Sanati, J. Mankowski, J. Dickens, A. A. Neuber, and R, P. Joshi, Physics of Plasmas **27**, 093511 (2020).
84. H. Nguyen, J. Mankowski, J. C. Dickens, A. A. Neuber, and R. P. Joshi, *Physics of Plasmas* **24**, 073505 (2017).
85. J. T. Krile, and A. A. Neuber, Appl. Phys. Lett. **98**, 211502 (2011).
86. I. A. Aponte, B. Esser, Z. C. Shaw, J. C. Dickens, J. J. Mankowski, and A. A. Neuber, Physics of Plasma **26**, 123512 (2019).
87. H. Nguyen, M. Sanati, and R. P. Joshi, J. Appl. Phys. **126**, 123301 (2019).
88. W. Pong, Journ. Appl. Phys. **40**, 1733 (1969).
89. Y. P. Raizer, *Gas Discharge Physics* (Springer, Berlin, 1997).
90. T. Ishikawa and R. B. McLellan, Journal of Physics and Chemistry of Solids **46**, 445 (1985).

91. W. G. Perkins and D. R. Begeal, Berichte der Bunsengesellschaft **76**, 863 (1972).
92. Y. Sakamoto and K. Takao, Journal of the Japan Institute of Metals **46**, 285 (1982).
93. Y. L. Liu, Y. Zhang, H. B. Zhou, G. H. Lu, F. Liu, G. N. Luo, Vacancy trapping mechanism for hydrogen bubble formation in metal, Phys. Rev. B **79**, 172103 (2009).
94. S. Kaufmann, Q. Shuai, D. J. Auerbach, D. Schwarzer, and A. M. Wodtke, The Journ. Chem. Phys. **148**, 194703 (2018).
95. P. N. Maya, Journal of Nuclear Materials **480**, 411 (2016).
96. For instance, X. Qiu, L. Diaz, M. Santi, J. Mankowski, J. Dickens, A. Neuber, and R. P. Joshi, Phys. of Plasmas **27**, 093511 (2020).
97. D. Gortat, P. T. Murray, S. B. Fairchild, M. Sparkes, T. C. Back, G. J. Gruen, M. M. Cahay, N. P. Lockwood, and W. O'Neil, Materials Letters **190**, 5 (2017).
98. J. M. D. Lane, K. Leung, A. P. Thompson, and M. E. Cuneo, J. Phys.: Condens. Matter **30**, 465002 (2018).
99. C.B. Duke in *Tunneling in Solids* (Academic Press, New York, 1969).
100. J. R. Harris, K. L. Jensen, D. A. Shiffler, and J. J. Petillo, Applied Phys. Lett. **106**, 201603 (2015).
101. P. O. Gartland S. Berge, and B. J. Slagsvold, Phys. Rev. Lett. **28**, 738 (1972).
102. H. K. A. Nguyen, M. Sanati, and R. P. Joshi, J. Appl. Phys. **126**, 123301 (2019).
103. G. Henkelman, A. Arnaldsson, and H. A. J´onsson, Comput. Mater. Sci. **36**, 354 (2006).
104. E. Sanville, S. D. Kenny, R. Smith, and G. Henkelman, J. Comp. Chem. **28**, 899 (2007).
105. W. Tang, E. Sanville, and G. Henkelman, J. Phys. Condens. Mater. **21**, 084204 (2009).
106. M. Yu and D. R. Trinkle, J. Chem. Phys. **134**, 064111 (2011).
107. P. O. Gartland, S. Berge, and B. J. Slagsvold, Phys. Rev. Lett. **28**, 738 (1972).
108. M. Chelvayohan and C. H. B. Mee, Journal of Physics C: Solid State Physics **15**, 2305 (1982).
109. J. Lecoeur, J. Bellier, and C. Koehler, Electrochimica Acta **35**, 1383 (1990).
110. E. Wimmer, A. J. Freeman, J. R. Hiskes, and A. M. Karo, Phys. Rev. B **28**, 3074 (1983).
111. B. Lesiak, A. Jablonski, J. Zemek, P. Jiricek, P. Lejcek, and M. Cernansk´y, Surf. Interface Anal. **30**, 217 (2000).
112. W. Dolinski, S. Mroz, J. Palczynski, B. Gruzza, P. Bondot, and A. Porte, ACTA Physica Polonica A **81**, 193 (1992).
113. H. Beilschmidt, I. S. Tiliuin, and W. S. M. Werner, Surface and Interface Analysis **22**, 120 (1994).
114. I. M. Bronstein and B. S. Fraiman, Vtorichnaya Elektronnaya Emissiya (Nauka: Movkva, 1969) p. 340.